The Optical Spectra of NiP, NiPz, NiTBP, and NiPc: Electronic Effects of *Meso*-tetraaza Substitution and Tetrabenzo Annulation

A. Rosa* and G. Ricciardi*

Dipartimento di Chimica, Università della Basilicata, Via N. Sauro 85, 85100 Potenza, Italy

E. J. Baerends* and S. J. A van Gisbergen

Afdeling Theoretische Chemie, Vrije Universiteit, De Boelelaan 1083, 1081 HV Amsterdam, The Netherlands

Received: September 27, 2000

Time-dependent density functional calculations have been performed on the symmetry and spin-allowed E_u excited states of the nickel tetrapyrrole series, NiP, NiPz, NiTBP, and NiPc. Optical spectra collected in noncoordinating solvents are presented for NiTBP, for the newly synthesized octaethyl nickel porphyrazine, NiOEPz, and for MgOEPz. The theoretical results prove to agree very well with the experimental data, providing an accurate description of the UV−vis spectra. The effects on the optical spectra of introducing in the basic porphyrinic ring, aza bridges, benzo rings, both aza bridges and benzo rings, and a transition metal are highlighted and interpreted on the basis of the electronic structure changes occurring along the series. The following results were found: (i) The near-degeneracy of the configurations ($a_{1u}e_g$) and ($a_{2u}e_g$) of the four-orbital model leads to strong mixing in NiP. The resulting low-energy state corresponds to the Q band with low intensity due to opposing transition dipoles of the contributing transitions. In NiTBP, NiPz, and NiPc, the degeneracy is lifted, and the lowest transition becomes increasingly purely ($a_{1u}e_g$) with concomitant larger intensities in the Q band, which is most intense in NiPc. (ii) The B band is calculated to correspond in NiP to a strong mixture of the degenerate ($a_{1u}e_g$) and ($a_{2u}e_g$) configurations with parallel transition dipoles, hence a large intensity. In NiPz and NiPc, the B band can no longer be described in terms of the four-orbital model, it has considerable MLCT character in NiPz and corresponds to a more complicated configuration mixing in NiPc. (iii) Transitions involving metal 3d states, either MLCT or LMCT, influence notably the spectrum to the blue of the B band.

1. Introduction

Since the middle of the century, the optical spectra of metal complexes with the most representative tetrapyrrole ligands, namely, porphyrins (P), porphyrazines (Pz), tetrabenzoporphyrins (TBP), and phthalocyanines (Pc), have been the subject of numerous experimental and theoretical studies. The vital role played by these systems in biological processes and their potential technological applications[1−3] strongly motivated this interest.

The changes in energy and intensity of the main UV−vis bands upon meso-tetraaza substitution and tetrabenzo annulation of the basic porhyrinic ring are to date well documented.[3−9]

Thus, for instance, porphyrazine, tetrabenzoporphyrin, and phthalocyanine complexes all exhibit a significant red shift in the energy and an intensification relative to the B (Soret) band of the lowest-energy $\pi \rightarrow \pi^*$ Q band.

The azamethine groups give rise to the possibility of additional $n \rightarrow \pi^*$ transitions which alter the spectra of porphyrazine and phthalocyanine compared to those of porphyrin and tetrabenzoporphyrin complexes, especially in the region of the Soret band.

The benzo groups give rise to more complicated $\pi \rightarrow \pi^*$ spectra for Pc and TBP than for P and Pz complexes. The different nature of the macrocycle is expected to reflect not only on the spectral features associated with ligand-centered electronic transitions but also on those involving the metal ion because of the differences in the metal−ligand interaction due to the different size of the coordination cavity.

Since the pioneering Pariser−Parr−Pople (PPP) calculations by Weiss et al.[9] on porphyrins and related systems, many theoretical studies have been devoted to the excited states of metalloporphyrins and metallophthalocyanines, most of them at a semiempirical level. The optical spectra of metalloporphyrazines and metallotetrabenzoporphyrins have received much less theoretical attention,[10−14] due to the paucity of experimental spectroscopic data for these systems whose bright future for applications was disclosed only recently.[15,16]

No theoretical effort has been put forth in the attempt to explain the dependency of the energy and intensity of the main UV−vis bands on the macrocycle framework as well as on the central metal, the only exception in this context being the SAC-CI (symmetry adapted cluster configuration interaction) calculations of the lowest excited states of free-base porphyrin,[17] free-base tetraazaporphyrin,[18] free-base phthalocyanine,[19] and the multireference Møller−Plesset perturbation (MRMP) calculations by Hashimoto et al.[20] of the lowest excited states of free-base porphin, and magnesium, zinc porphyrins, and related molecules.

With the aim of quantifying the effects on the optical spectra of introducing a basic porphyrinic ring, aza bridges, benzo rings, both aza bridges and benzo rings, and a transition metal, we study here the excited states of the nickel tetrapyrrole series, NiP, NiPz, NiTBP, and NiPc, using time-dependent density

10.1021/jp003508x CCC: $20.00
Published on Web 03/09/2001

functional theory (TDDFT). TDDFT provides a first-principles method for the calculations of excitation energies and many related response properties within a density functional context.

For applications to large molecules, TDDFT methods are an excellent alternative to conventional highly correlated ab initio methods such as SAC−CI, STEOM-CC (similarity transformed equation-of-motion coupled cluster), and CASPT2 (complete active space SCF plus second-order perturbation theory), for which calculations of the excited states of transition metal tetrapyrroles are still a challenge. The reliability of the TDDFT approach in obtaining accurate predictions of excitation energies and oscillator strengths is by now well documented for a wide range of molecules, ranging from small molecules[21−25] to large organic molecules,[26,27] higher fullerenes,[28] and, more recently, metal carbonyls,[29,30] free-base porphin,[31] and transition-metal tetrapyrrole sandwiches.[32] TDDFT usually provides an accuracy for excitation energies comparable to that of the most advanced ab initio methods.

Gas-phase spectra to which to compare our theoretical results are available for NiPc[7] and the octaethyl substituted nickel-porphyrin, NiOEP.[33] Solution spectra have been reported to date for NiPz and NiTBP, but these are not suitable for comparison with theory since, due to the poor solubility of these macrocycles in most organic solvents, the spectra have been taken in coordinating solvents, which strongly affects the intensity and energy of the main bands. To have experimental data more suitable for comparison, we have collected in diluted solutions of noncoordinating solvents the optical spectra of the tetrabenzo porphyrin Ni(II) complex and of the newly synthesized octaethyl substituted nickel porphyrazine, NiOEPz. With the aim to clarify the effect of the presence of the d shell on the B−N band system of metal-porphyrazines, we have also performed calculations on the excited states of a nontransition metal porphyrazine, MgPz. The theoretical results are compared with the optical spectrum of the ad hoc resynthesized magnesium octaethylporphyrazine, MgOEPz, taken in a diluted solution of a noncoordinating solvent.

The interpretation of the spectral changes along the series, of such important features as the relative intensitities of the Q and B band systems, of the additional features (N, L, and "extra bands"), and of the influence of the metal 3d states relies heavily on a detailed analysis of the electronic structure of these systems. We will elucidate the electronic structure effects of introducing in the basic porphyrinic ring aza bridges, (NiP → NiPz), benzo rings, (NiP → NiTBP), and both aza bridges and benzo rings, (NiP → NiPc) using a fragment approach where the four pyrrole or indole rings and the methine or aza bridges are taken as building blocks. The extensive molecular orbital analysis we present here provides not only a new and more clear picture of the electronic structure of the title tetrapyrrole complexes but also a powerful tool to predict the changes in energy and intensity of the spectral features upon variation of the macrocycle framework or addition of electron donating or electron accepting peripheral substituents. We wish to stress that the Kohn−Sham molecular orbitals on which our electronic structure analysis is based are physically meaningful (see refs 34 and 35 and references therein). This is related to the fact that the effective local potential of the Kohn−Sham model has as leading terms—apart from the nuclear potential and Coulomb potential of the total electronic density—the potential due to both the Fermi (exchange) hole and the Coulomb hole.[35−37] The latter builds in effects of electronic correlation and in fact gives the Kohn−Sham MOs an advantage over the Hartree−Fock orbitals in cases of strong near-degeneracy correlation. Virtual Kohn−Sham orbitals, being solutions in exactly the same potential as that of the occupied orbitals, have the advantage that they lack the artificial upshift and diffuse character of Hartree−Fock orbitals. The virtual-occupied Kohn−Sham orbital energy differences $\Delta\epsilon_{ia} = \epsilon_a - \epsilon_i$ are in the TDDFT approach the zeroth-order approximation to the excitation energies. All these properties make the Kohn−Sham orbital model very suitable for interpretation of the electronic structure and elucidation of the character of the excitations. The meaning of Kohn−Sham orbitals and their use for interpretation of chemical bonding is extensively discussed in ref 38. The use of Kohn−Sham orbitals affords a direct connection with the many LCAO-MO treatments based on semiempirical or Hartree−Fock orbitals, while having at the same time the benefit of the high accuracy of the time-dependent DFT tratment of the excitation energies.

2. Method and Computational Details

The computational method we use is based on the time-dependent extension of density functional theory. TDDFT is thoroughly reviewed in refs 21 and 39−41. In our implementation,[42,43] the solution of the TDDFT response equations proceeds in an iterative fashion starting from the usual ground-state or zeroth-order Kohn−Sham (KS) equations. For these, one needs an approximation to the usual static exchange-correlation potential $v_{xc}(\mathbf{r})$. After the ordinary KS equations have been solved, the first-order density change is calculated from an iterative solution to the first-order KS equations.[42] In these first-order equations, an approximation is needed to the first functional derivative of the time-dependent exchange-correlation potential $v_{xc}(\mathbf{r}, t)$ with respect to the time-dependent density $\rho(\mathbf{r}',t')$,[40,44,45] the so-called exchange-correlation (xc) kernel.

For the xc kernel, we use the adiabatic local density approximation (ALDA). In this approximation, the time dependence (or frequency dependence if one talks about the Fourier transformed kernel) is neglected, and one simply uses the differentiated static LDA expression. In our case, we use the Vosko−Wilk−Nusair parametrization.[46] This approximation is computationally efficient, and it has been demonstrated that other existing approximations do not improve upon the ALDA xc kernels.[23−26,47]

For the exchange-correlation potentials which appear in the zeroth-order KS equations, we use the recent model KS exchange-correlation potential v_{xc}^{SAOP}, which is constructed with a statistical average of different model potentials for occupied KS orbitals (SAOP).[48,49] This potential by construction provides a balanced description of the electron exchange and correlation in both outer and inner atomic and molecular regions. High-quality results for a wide variety of response properties of prototype molecules have been recently obtained using v_{xc}^{SAOP}.[49] Excited-state calculations have also been performed using the more popular generalized gradient approximated (GGA) potential v_{xc}^{BP}, employing Becke's gradient approximation for exchange[50] and Perdew's for correlation.[51] BP results, not reported here, are generally very similar to SAOP results, except for MLCT and LMCT excited states which are computed at the BP level at energies lower than those at the SAOP level as a consequence of the observed upshift of the metal based molecular orbitals on going from the SAOP to BP potential. This leads in some cases to a different description of the excited states, the SAOP results appearing to be more in line with the experiment than BP results. Relevant examples of these differences will be given in the following.

The calculations have been performed for the spin-allowed singlet A_{2u} and E_u excited states in the energy range covered

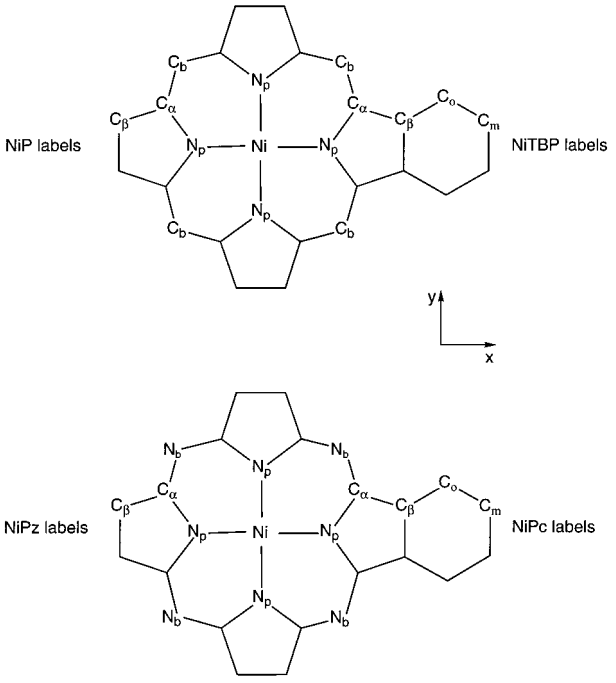

Figure 1. Atom labeling scheme for NiP (top, left side), NiTBP (top, right side), NiPz (bottom, left side), and NiPc (bottom, right side).

by the experimental spectra, but only the E_u states will be reported and discussed in this paper. The A_{2u} excitations up to 5.0 eV have oscillator strengths smaller than 1.0×10^{-3} and are therefore not relevant for the interpretation of the main spectral features of the investigated metallomacrocycles.

All calculations reported in this paper have been performed with the ADF-RESPONSE module[43] which is an extension of the Amsterdam density functional (ADF) program system.[52−54]

For the calculations we made use of the standard ADF IV basis set,[55] which is an uncontracted triple-ζ STO basis set, with one 3d polarization function for C and N atoms, one 3p and one 3d for the Mg atom, one 2p for H atoms, and a triple-ζ nd, (n+1)s basis with one (n+1)p function for Ni. The cores (C and O, 1s; Mg and Ni, 1s-2p) were kept frozen.

The calculations of the excited states have been performed for the ground-state geometries of the molecules optimized at BP level imposing D_{4h} symmetry. The molecules lie in the *xy* plane, with the *x*- and *y*-axes passing through pyrrolic nitrogens (cf. Figure 1). Selected optimized structural data of the investigated Ni(II) tetrapyrrole series, together with the recent high-quality X-ray data of NiP,[56] are reported in Table 1 (see Supporting Information). The excellent agreement between the optimized and experimental geometrical parameters of NiP while confirming the validity of nonlocal density functional methods in predicting the molecular structures of porphyrinic systems supports the reliability of our optimized structures for the other members of the series.

3. Experimental Section

Materials. A sample of pure NiTBP was kindly provided by Professor Noboru Ono, Ehime University, Matsuyama, Japan. The synthesis and the characterization data of the complex are reported in ref 57.

N,*N*-Dimethylformamide (DMF, Aldrich), hexane, and dichloromethane (Fluka) were of spectroscopic or HPLC grade and used without further purification. Nickel chloride dimethoxyethane adduct, $NiCl_2$·DMOE, was a STREM product. Magnesium turnings used in the synthesis of MgOEPz were from Aldrich.

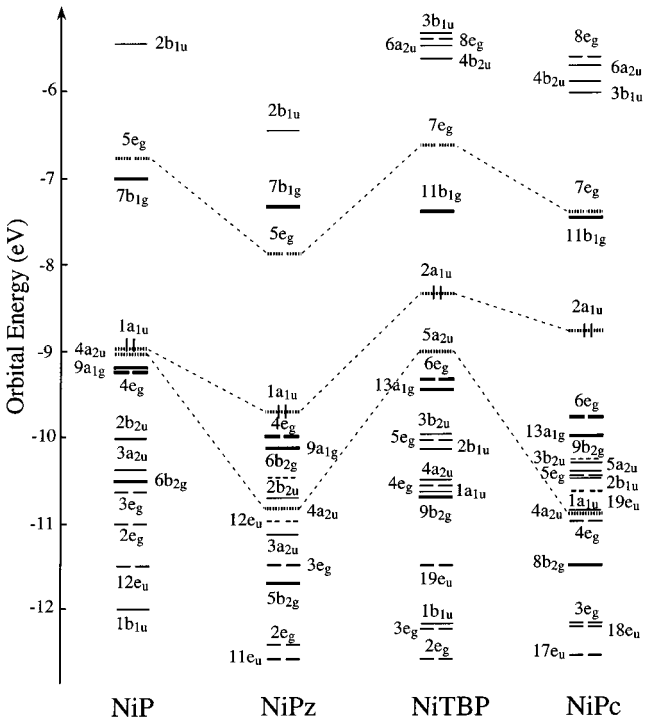

Figure 2. Energy level scheme for NiP, NiPz, NiTBP, and NiPc. Double occupancy is indicated for the HOMO only. All lower-lying levels are also doubly occupied. The metal 3d orbitals are indicated with heavy lines, the four Gouterman orbitals are indicated with hatched lines, and the N_b lone pair orbitals of b_{2g} and e_u symmetry are indicated with dashed lines.

The elemental analyses were provided by the Microanalysis Laboratory of the Inorganic Department of the University of Padova (Italy).

Spectroscopic and Physical Measurements. Solution electronic absorption spectra were recorded at room temperature with a Cary 05E spectrophotometer. The solvents were dichloromethane for NiTBP and hexane for MgOEPz and NiOEPz. NiTBP was dissolved in dichloromethane by prolonged sonication at room temperature under vigorous stirring.

ESI mass spectra were obtained with a LCQ (Finningan MAT) spectrometer.

Syntheses. *H_2OEPz.* The free-base porphyrazine, H_2OEPz, was prepared and characterized according to the method of Fitzgerald et al.[16]

MgOEPz. The synthesis of MgOEPz was previously reported.[16] ES^+ MS (chloroform, *m*/*z*): theory, 562 (MH^+); found, 562 (MH^+). Anal. Calcd. for $C_{32}H_{40}N_8Mg$: C, 68.50; H, 7.19; N, 19.97. Found: C, 68.37; H, 7.10; N, 19.55.

NiOEPz. H_2OEPz (13 mg, 0.024 mmol), $NiCl_2$·DMOE (50 mg, 0.23 mmol), and 2,4,6-trimethylpyridine (1 drop) were dispersed in a mixture of dichloromethane (5 mL) and DMF (3 mL). The slurry was stirred and heated at 100 °C for 31 h. The solvents were removed under vacuum, and the resulting dark blue powder was passed down to a silica gel column (Merk Kieselgel 60 270−400 mesh) using a 9:1 chloroform/ethanol mixture as eluant (first band). Yield, 97%. ES^+ MS (chloroform, *m*/*z*): theory, 596 (MH^+); found, 596 (MH^+). Anal. Calcd. for $C_{32}H_{40}N_8Ni$: C, 64.55; H, 6.77; N, 18.82. Found: C, 64.60; H, 6.57; N, 18.50.

4. Electronic Structure Analysis

In Figure 2, the highest occupied and the lowest unoccupied ground-state one-electron levels are shown for the whole series.

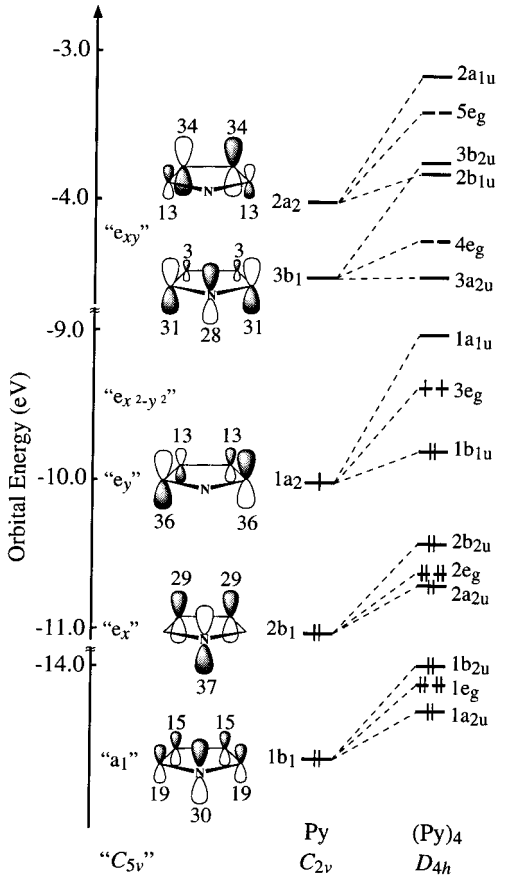

Figure 3. Orbitals and orbital energies of the pyrrolic ring system. The contributions of the individual C p_z atomic orbitals to the MOs, in percentages based on Mulliken gross orbital populations per MO, are indicated in the Figure. The orbital levels in the $(Py)_4$ cage are also given.

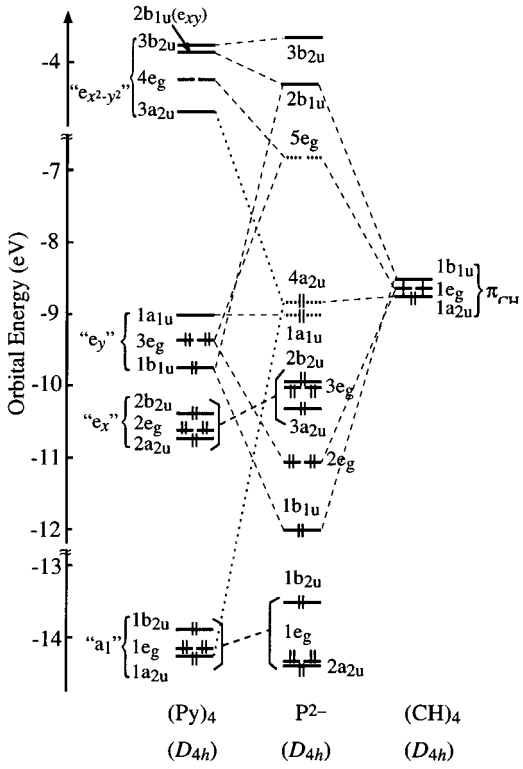

Figure 4. Orbital interaction diagram for interaction between the $(Py)_4$ cage and the four CH methine bridges. Gouterman's four orbitals ($1a_{1u}$, $4a_{2u}$, $5e_{g,xz}$, and $5e_{g,yz}$) are indicated with hatched lines. The orbital numbering of the P ring system has been adapted to the situation in metal salts (see Figure 2), where a metal $3d_\pi$-$4e_g$ is present above the P-$3e_g$ and a metal $3p_z$-$1a_{2u}$ is present below the P-$2a_{2u}$.

For sake of clarity, the metal 3d orbitals in this figure are indicated with heavy lines, the important four orbitals for the Q and B bands, which we will simply denote as the "Gouterman orbitals", are indicated with hatched lines, and the N_b (bridging nitrogen) lone pair orbitals of b_{2g} and e_u symmetry are indicated with dashed lines.

Most of the features of the orbital level spectrum and the underlying electronic structure of the ring systems can be understood from a fragment approach where the four pyrrole or indole rings and the methine or aza bridges are taken as building blocks.

Electronic Structure of Porphin. The pyrrolic rings are basically cyclopentadiene (Cp) rings perturbed by the N substitution in the five-ring. Referring to the C_{5v} nomenclature appropriate for the Cp ring, we note that the pyrrolic π electron system is characterized by a lowest A_1 combination, with, however, a relatively large weight on the more electronegative N atom (see Figure 3), followed by the E_1 set of orbitals, which are no longer degenerate, the "e_x" partner with its amplitude on N (and on the C_β Carbon atoms) being more stabilized (by 1.12 eV) than the "e_y" partner with N in its nodal plane and high amplitude on the C_α atoms. The distinguishing feature of the e_x and e_y orbitals is the different amplitude on the C_α atoms to which the methine or aza bridges will attach. The nodal plane of the e_x orbital passes practically through the C_α atoms, which therefore have no amplitude, so we may expect little interaction with the methine or aza bridges. On the other hand, the e_y orbitals with their large C_α amplitudes will strongly interact with the bridges. The E_2 orbitals finally are also split by the N perturbation, but less so (only 0.55 eV) than the E_1 set. The "$e_{x^2-y^2}$" has relatively large amplitude on C_α and may therefore play a role in the interaction with the bridges.

When forming the $(Py)_4$ cage, without bridges present, the MOs of the Py rings form the symmetry combinations as indicated in Figure 3. Evidently, the high C_α amplitudes lead to significantly more overlap and energy dispersion for the e_y and $e_{x^2-y^2}$ orbitals than for the other ones.

We next consider the interaction of the $(Py)_4$ orbitals with methine and aza bridges in Figures 4 and 5, respectively. Note that we take as the electron count for the $(Py)_4$ cage 22 electrons the four times five π electrons for the rings being supplemented with two electrons, in accordance with the charge of 2− for the ring system in metal salts, or with the two additional electrons coming from the in-plane hydrogen atoms in free base porphin. A notable feature in the interaction diagram for $(Py)_4$ with $(CH)_4$ in Figure 4 is that the e_x orbitals, with their lack of amplitude on C_α, are very little affected by the bridges and carry over almost unperturbed to the porphin ring system. The $2b_{2u}$, $3e_g$, $3a_{2u}$ set of e_x orbitals can be clearly recognized in the levels of the metal salt in Figure 2. We have for the ease of comparison adopted the same orbital numbers in Figures 4 and 5 as those in the NiP (and NiPz) systems in Figure 2, so the numbers of the a_{2u} orbitals of P in Figure 4 have been raised by 1 to account for the presence of the metal $3p_z$-a_{2u} orbital below the π orbitals of P in the numbering of Figure 2, and the first virtual e_g orbital has been numbered $5e_g$ since the Ni-$3d_\pi$ orbital is inserted, as $4e_g$, above the $3e_g$ in the NiP systems. Comparing NiP in Figure 2 with the P levels in Figure 4, we note that the presence of the metal ion does not disturb the e_x set of orbitals very much; only the $3e_g$ is pushed down, to below the $3a_{2u}$, by the metal $3d_\pi$-$4e_g$, and a metal orbital ($3d_{xy}$-$6b_{2g}$) is inserted in the e_x set. The

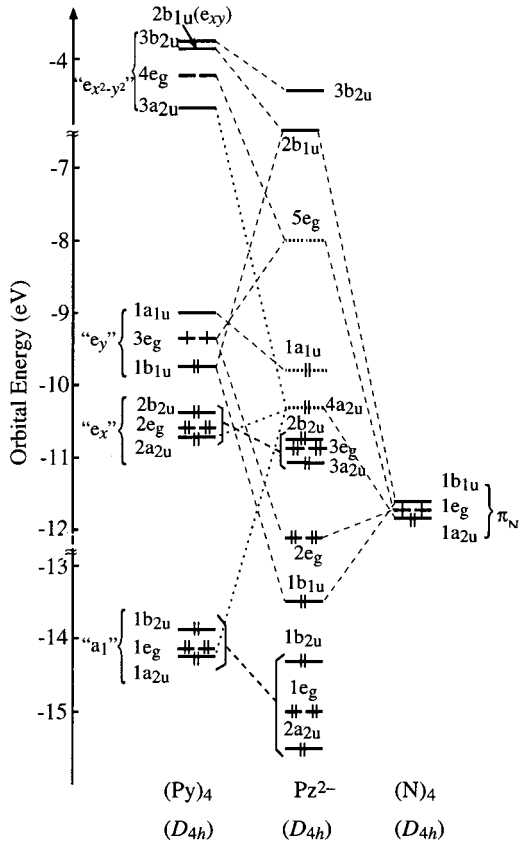

Figure 5. Orbital interaction diagram for interaction between the $(Py)_4$ cage and four N bridging atoms. Details as the same as those in Figure 4.

plot of the $3a_{2u}$ orbital of NiP in Figure 6 nicely demonstrates its e_x origin, with large amplitudes at the pyrrolic nitrogens and (with opposite sign) at the C_β atoms.

Contrary to the e_x orbitals, the e_y orbitals exhibit strong interaction with the CH bridges. The $(Py)_4$ $3e_g$-e_y and $1b_{1u}$-e_y orbitals show interaction with orbitals of matching symmetry in the set of $(CH)_4$ π orbitals, resulting in large gaps between the bonding and antibonding combinations. The antibonding ones, $5e_g$ and $2b_{1u}$, actually rise so high as to come close to the $e_{x^2-y^2}$ and e_{xy} type of orbitals and are stabilized by admixture of these. The $5e_g$ LUMO is of course important for the low-lying excitation energies. Interestingly, the two highest occupied orbitals are also derived from the e_y and π_{CH} orbitals, but from the two orbitals, $1a_{1u}$ on $(Py)_4$ and $1a_{2u}$ on $(CH)_4$, that find no partner on the other system. These therefore end up in P as "nonbonding" orbitals at almost unchanged energies. The $1a_{1u}$ has nodal planes through the CH bridges and is virtually a 100% $(Py)_4$-e_y orbital. Its e_y origin and lack of amplitude at the bridges are evident from the orbital plot of $1a_{1u}$ of NiP in Figure 6. The $4a_{2u}$ is an in-phase combination of the π orbitals on the C atoms of the CH bridges (the A_{2u} irrep is only antisymmetric with respect to the plane of the molecule). It does in fact have significant admixture of the $3a_{2u}$ and $1a_{2u}$ $(Py)_4$ orbitals (23% and 14% respectively), which both have amplitudes at C_α. The lack of C_α character prevents the $(Py)_4$ e_x-$2a_{2u}$ from getting involved. It is easily deduced from the phases with which the $3a_{2u}$-$(Py)_4$ and $1a_{2u}$-$(Py)_4$ will mix with the $1a_{2u}$-$(CH)_4$ that the amplitudes on the pyrrolic N_p will reinforce each other; the amplitudes at C_α, however, interfering destructively. The plot of the $4a_{2u}$ of NiP in Figure 6 indeed exhibits, in addition to the strong amplitude at the CH bridges of this originally $(CH)_4$ orbital, considerable amplitude with reversed sign at the N_p.

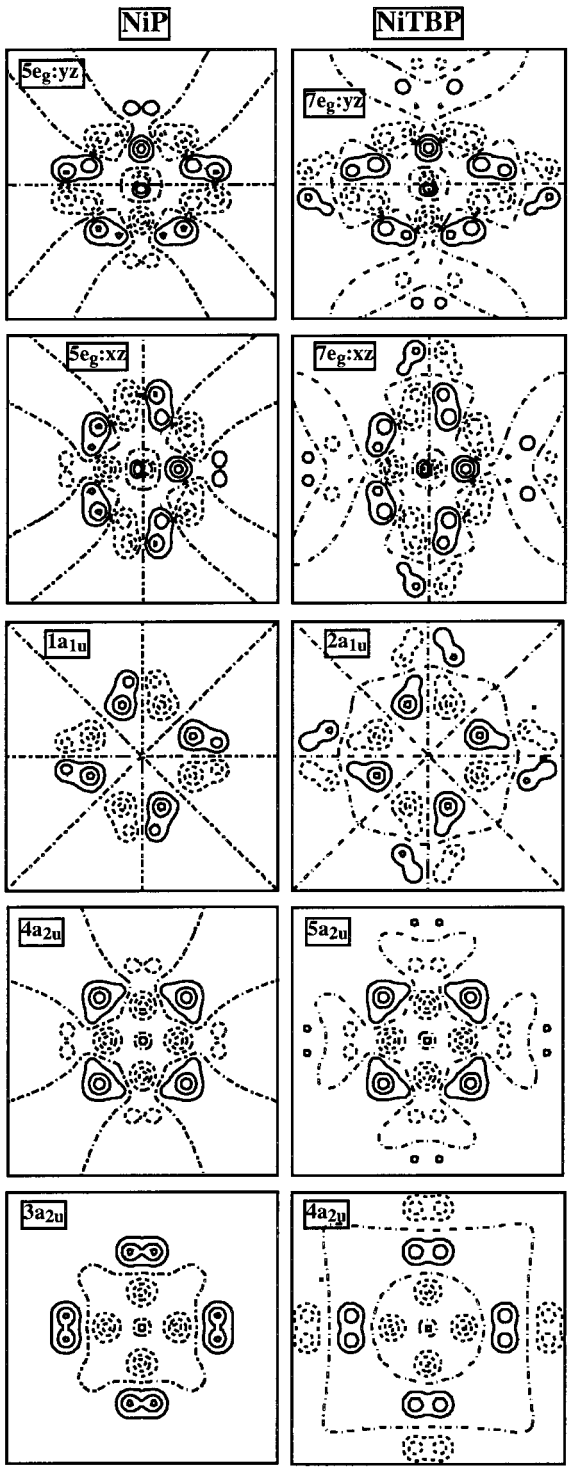

Figure 6. Contour plots of the $1a_{1u}$, $3a_{2u}$, $4a_{2u}$, $5e_{g,xz}$, and $5e_{g,yz}$ orbitals of NiP and of the $2a_{1u}$, $4a_{2u}$, $5a_{2u}$, $7e_{g,xz}$, and $7e_{g,yz}$ orbitals of NiTBP. The plane of drawing is 0.3 bohr above the molecular plane. Contour values are 0.0, $\pm$0.02, $\pm$0.05, $\pm$0.1, $\pm$0.2, and $\pm$0.5 $[e/bohr^3]^{1/2}$.

The plots of Figure 6 further demonstrate that the $5e_g$ orbitals consist of antibonding combinations of the $(Py)_4$ e_y-$3e_g$ (37%) with the $(CH)_4$ $1e_g$ (29%), stabilized by the $(Py)_4$ $e_{x^2-y^2}$-$4e_g$ (27%). The e_y-$3e_g$ and $e_{x^2-y^2}$-$4e_g$ are localized on different sets of Py rings; for instance, $e_{g,xz}$ combinations are formed with e_y orbitals on Py rings at the *y* axis and with $e_{x^2-y^2}$ orbitals on the Py rings at the *x*-axis. Admixture of $e_{x^2-y^2}$-$4e_g$ thus brings in amplitude on the N_p and C_α atoms of the two other Py rings than the ones where e_y-$3e_g$ was located (cf. Figure 6).

The highest occupied orbitals $1a_{1u}$ and $4a_{2u}$ and the lowest unoccupied orbitals $5e_{g,xz}$ and $5e_{g,yz}$ are the four orbitals whose significance for the UV and visible absorption spectrum have been stressed by Gouterman.[58] To understand the intensities of the transitions, it is important to notice that these orbitals all derive from the same orbitals at the $(Py)_4$ side (the e_y set) and the $(CH)_4$ side (the π_{CH} orbitals). This means that when a transition dipole matrix element is nonzero by symmetry, it will usually be large since the intraunit (on one Py fragment or on one CH fragment) contributions will be large. We may take as an example the *y*-components of the E_u excited states, ignoring spin for the moment (i.e., assuming the electrons to be singlet coupled). Both the $1a_{1u} \rightarrow 5e_g$ and the $4a_{2u} \rightarrow 5e_g$ excitations lead to E_u states, the E_u *y*-components being $1e_{u,y} = 1a_{1u}5e_{g,xz}$ and $2e_{u,y} = 4a_{2u}5e_{g,yz}$. The transition dipole $\langle 1a_{1u}|y|5e_{g,xz}\rangle$ is large because the $1a_{1u}$ consists of e_y orbitals on $(Py)_4$ while $5e_{g,xz}$ also has, apart from the antibonding π_{CH} contribution, e_y character, namely, on the Py groups at the positive and negative *y*-axes (see Figure 6). The on-site overlaps (on these Py fragments) are large. The multiplication with *y* ensures that the signs are such that constructive interference occurs. The other transition dipole, $\langle 4a_{2u}|y|5e_{g,yz}\rangle$, is large because both $4a_{2u}$ and $5e_{g,yz}$ are derived from the same set of orbitals, i.e., π_{CH}. We may expect the transition dipole to be somewhat less than that for $\langle 1a_{1u}|y|5e_{g,xz}\rangle$ since the $4a_{2u}$ has less π_{CH} content (59%) than $1a_{1u}$ has e_y content (98%) and since $5e_{g,yz}$ has less π_{CH} content (29%) than $5e_{g,xz}$ has e_y content (37%). The situation is actually more favorable for $\langle 4a_{2u}|y|5e_{g,yz}\rangle$ than this comparison suggests, since the N_p p_z character that both the $4a_{2u}$ (due to the $(Py)_4$-$3a_{2u}$ and $(Py)_4$-$1a_{2u}$ admixtures, see above) and the $5e_{g,yz}$ (due to $(Py)_4$-$4e_{g,yz}$ admixture) acquire is helpful for building a large dipole matrix element, as may be easily deduced from the phases as depicted in Figure 6. We find numerically in NiP the large value of ca. 3.25 au for $\langle 1a_{1u}|y|5e_{g,xz}\rangle$. The $\langle 4a_{2u}|y|5e_{g,yz}\rangle$ matrix element is, with ca. 2.92 au, actually not much smaller. In free-base porphin, the analogous values are 3.30 and 2.72 au, respectively.

For excitations out of the e_x-derived set of orbitals, $2b_{2u}$, $3e_g$, and $3a_{2u}$, to $5e_g$ orbitals, the transition dipole matrix elements will suffer from a "zero-order" vanishing of the matrix elements due to the zero on-site overlap between a Py-e_x and a Py-e_y orbital. The actual transition dipoles will not be zero (except for $3e_g \rightarrow 5e_g$, where they are zero by symmetry) since the e_x orbitals have large N_p amplitude, while we have seen that $5e_g$ also acquires some N_p character. In addition, the π_{CH} character of $5e_g$ works favorably by way of overlap with N_p-p_z amplitude in the e_x derived set. Nevertheless, we find dipole matrix elements that are smaller by factors between 3 and 20 compared to the large dipole matrix elements for the Gouterman transitions.

The proximity of the $1a_{1u}$ and $4a_{2u}$ levels suggests near-degeneracy of the two primary E_u excited states derived from the $(1a_{1u}5e_g)$ and $(4a_{2u}5e_g)$ configurations. In case of accidental degeneracy or near-degeneracy already, a small coupling matrix element will induce strong mixing, close to 50:50. There is vast literature on the importance of this configuration interaction between the $(1a_{1u}5e_g)$ and $(4a_{2u}5e_g)$ configurations. The phases of the mixing coefficients and the transition dipoles are such that the low-energy stabilized linear combinations, accounting for the Q band in the visible spectrum, have low intensity due to opposite directions of the two large transition dipoles while the high-energy out-of-phase linear combinations, accounting for the B or Soret band in the UV, have parallel transition dipoles and therefore a large overall transition dipole, i.e., high intensity. A qualitative understanding of the main spectral features of the porphin spectra is thus obtained straightforwardly. We should of course be aware of the possibility of further configuration interaction, which will in practice bring contributions from e_x to $5e_g$ transitions (the $2b_{2u} \rightarrow 5e_g$ and $3a_{2u} \rightarrow 5e_g$ being the only allowed ones) but also from, for instance, $3e_g \rightarrow 2b_{1u}$ and other transitions. We will consider in the next section the detailed results of the calculations.

In a forthcoming paper,[59] we will consider the connection of our presentation in terms of pyrrolic fragments and CH bridges with the interpretation of the porphin spectra starting from a cyclic polyene model system, which has historically played a large role[60−62] and is still often cited as providing a qualitative basis for our understanding of the weak Q and strong B band system of porphyrines.

Comparison of the Pyrrolic Ring Systems with Benzopyrrolic Systems. In NiTBP, we observe in the level diagrams of Figure 2 as most conspicuous changes with respect to NiP the destabilization of the a_{1u} HOMO, no longer (nearly) degenerate with the a_{2u}, and the introduction in the virtual spectrum of additional low-lying π^* levels, such as the $4b_{2u}$, the $6a_{2u}$, and the $8e_g$, close to the $3b_{1u}$, which is the analogue of the $2b_{1u}$ of the P and Pz systems. The highest occpied a_{2u} is not much affected, compare the $5a_{2u}$ in NiTBP with the $4a_{2u}$ in NiP. This would be understandable if the $2a_{1u}$ is again mostly a (benzo)pyrrolic orbital and the $5a_{2u}$ mostly a $(CH)_4$ orbital. To understand the effect of the benzo rings, we show in Figure 7 contour plots of the lowest π orbitals of the benzopyrrole ring system (BzPy). The levels are also given in this figure. The lowest orbital, the nodeless $1b_1$, is a low-energy in-phase combination of the C $2p_\pi$ AO's on the pyrrole and benzo rings. The single-node orbitals $2b_1$ and $1a_2$ (we only consider the vertical nodal planes) have e_x and e_y character on the pyrrole part and are stabilized by bonding admixtures of C $2p_\pi$ on the benzo part. The latter two orbitals are not expected to be degenerate, but their energy separation is doubtless increased by the stabilizing effect of the N_p on $2b_1$. The next higher orbitals, $3b_1$ and $2a_2$, have two vertical nodal surfaces. When considering their character in the pyrrolic ring part of BzPy, it is clear that these orbitals are analogous to the e_x of Py (the $3b_1$) and e_y of Py (the $2a_2$). Note the strong amplitude of $2a_2$-e_y at the C_α positions (62% total C_α-p_π character) and its higher energy due to the lack of amplitude at N_p. The $3b_1$-e_x has a nodal surface passing very close to the C_α, and it has a mere 3% total C_α-p_π character. There is a second nodal surface in these orbitals between the Py and the Bz parts, accounting for the higher energy of these orbitals as compared to the e_x and e_y orbitals of Py. In fact, they may be considered as antibonding combinations of the e_x and e_y orbitals of Py with Bz orbitals with high amplitude at the C_m carbons, the lower lying $2b_1$ and $1a_2$ being the Py-Bz bonding counterparts. We have therefore denoted in Figure 7 the $1a_2$ as "e_{y^+}" and $2a_2$ as "e_{y^-}" (sometimes just e_y) and the $2b_1$ and $3b_1$ as "e_{x^+}" and "e_{x^-}" (or just e_x)**.** The next higher pair of orbitals, $4b_1$ and $3a_2$, have in the Py part a strong resemblance to the $e_{x^2-y^2}$ and "e_{xy}" orbitals of Py.

We can now understand that, apart from the upward shift of the orbitals compared to Py, the BzPy will electronically behave very much analogously to Py. Our analysis of the electronic structure of P therefore applies to a large extent to TBP as well. The orbital energy diagram for $(BzPy)_4$ of Figure 7, for instance, displays such a feature as the larger dispersion of the e_{y^-}-derived set compared to the e_{x^-}-derived one. The interaction with $(CH)_4$, according to the orbital interaction diagram of Figure 7, again yields a pure BzPy-localized $2a_{1u}$ and a $(CH)_4$-localized a_{2u}

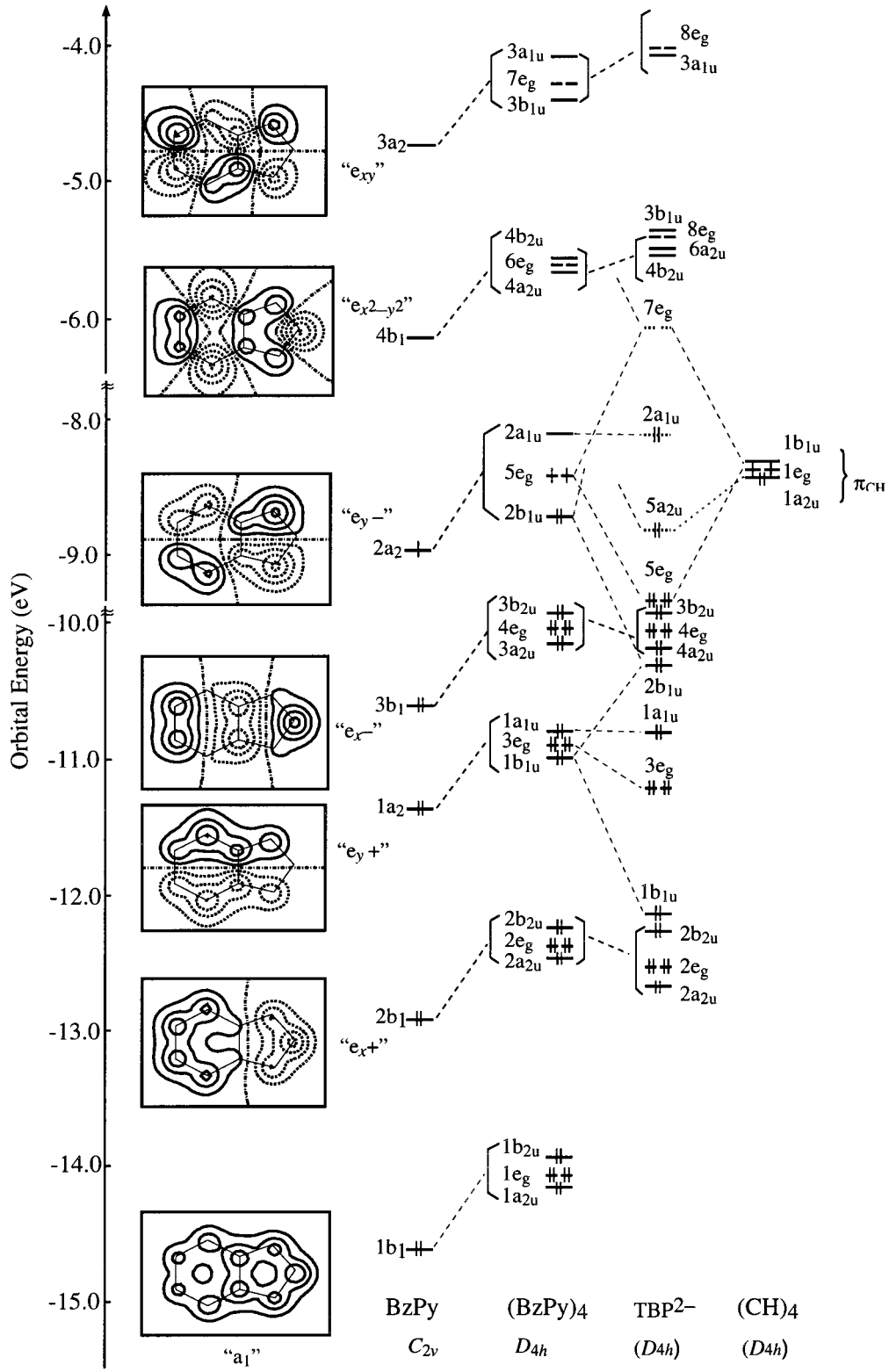

Figure 7. Orbital interaction diagram for interaction between the $(BzPy)_4$ cage and the four CH methine bridges. Contour plots and orbital energies of the lowest π orbitals of the benzopyrrolic fragment, BzPy, are also given. The plane of drawing is 0.3 bohr above the molecular plane. Contour values are 0.0, ±0.02, ±0.05, ±0.1, ±0.2, ±0.5 $[e/bohr^3]^{1/2}$.

(becoming $5a_{2u}$ in the NiTBP system). It is important that the $2a_{1u}$ is now at higher energy, which is a direct consequence of the higher energy of $2a_2$-e_y^- in BzPy and $2a_{1u}$-e_y^- in TBP, which are 1 eV higher in energy than $1a_2$-e_y in Py and $1a_{1u}$-e_y in $(Py)_4$, respectively. The $2a_{1u}$ is no longer degenerate with $5a_{2u}$ (see Figure 2), since this $(CH)_4$-based orbital stays at the same energy in the P and TBP ring systems. Figure 7 makes it easy to understand the orbital-level spectrum of NiTBP as presented in Figure 2, which will be the basis for the discussion of the absorption spectrum in the next section. In the energy range of −10 to −11 eV, there are in NiTBP six π levels, as compared to three in NiP. The e_x^--derived orbitals $3b_{2u}$, $4e_g$, and $4a_{2u}$ correspond to the e_x-derived orbitals ($2b_{2u}$, $3a_{2u}$, and $3e_g$) of NiP. In addition, there are the $5e_g$, $2b_{1u}$, and $1a_{1u}$. The $1a_{1u}$, the lowest of this set of orbitals, is a purely e_y^+-derived orbital, easily recognizable as such in Figure 7. The $5e_g$ and $2b_{1u}$ levels are

bonding BzPy-e_y^- to $(CH)_4$ orbitals. Their counterparts in P^{2-}, $2e_g$ and $1b_{1u}$ (see Figure 4), were positioned at considerably lower energies (see also the $2e_g$ and $1b_{1u}$ NiP levels in Figure 2). In NiTBP, the $5e_g$ and $2b_{1u}$ are at higher energies because of the upshift of e_y^-, which also caused $2a_{1u}$ to be higher than $5a_{2u}$. Moreover, the presence of the e_y^+ orbitals of e_g and b_{1u} symmetry pushes the $5e_g$ and the $2b_{1u}$ up so as to put them in the energy range of the e_x^- set. Comparing the ordering of the levels in Figures 2 and 7, one notes that in the Ni complex the $5e_g$ has shifted a little bit down, to below the $3b_{2u}$, and in particular the e_x^-derived $4e_g$ is stabilized, to below the e_x^--derived $4a_{2u}$ and close to the e_y^+-derived $1a_{1u}$. This is a consequence of the introduction of the 3d levels of Ni. The $5e_g$ orbitals have little overlap with the Ni $3d_{xz}$ or $3d_{yz}$ because they lack amplitude at the pyrrolic N and have to overlap with the Ni $3d_\pi$ orbital sideways. They are very little stabilized by Ni 3d. On the other hand, the e_x^--derived $4e_g$ (see BzPy-$3b_1$ in Figure 7) does have strong N_p character and a good π overlap with the lobes of the $3d_\pi$ orbital directed toward it (i.e., $3d_{xz}$ with the $3b_1$ in Figure 7). The $4e_g$ is in fact pushed down by Ni $3d_\pi$ to close to the e_y^+-derived $1a_{1u}$.

The $7e_g$ LUMO arises from antibonding interaction of the $5e_g$-e_y^- of $(BzPy)_4$ with the $(CH)_4$ $1e_g$. It will be stabilized by the $6e_g$-$e_{x^2-y^2}$ of $(BzPy)_4$, again very much like in the $(Py)_4$ with $(CH)_4$ interaction. It is instructive to consider the orbital plots for NiTBP in the panels to the right in Figure 6. It is clear that the NiTBP orbitals are, on the Py rings and CH bridges, indeed very similar to their counterparts in NiP. The arguments concerning the strengths of transition dipoles between the orbitals therefore carry over to the NiTBP case. It is the differences in the orbital energies, such as the lack of $5a_{2u}/2a_{1u}$ degeneracy, that will cause differences in the amount of configuration mixing and, therefore, in the transition intensities.

Electronic Structure of Azaporphyrins. The aza bridges introduce in the valence region a few levels that have in-plane N_b lone-pair character, namely, the $6b_{2g}$ and $12e_u$ in NiPz and the $9b_{2g}$ and $19e_u$ in NiPc, see the dashed levels in Figure 2. The further discussion is restricted to the π levels.

Figure 5 displays the orbital interaction diagram for $(Py)_4$ interaction with $(N)_4$. The interaction pattern is very similar to the one for the interaction with $(CH)_4$; in particular again, the e_x set of $(Py)_4$ orbitals has little interaction with the bridging N atoms, and the e_y set strongly interacts, resulting in a large gap between the bonding $1b_{1u}$ and $2e_g$ orbitals and the antibonding partners $5e_g$ and $2b_{1u}$. The latter are stabilized by admixture of the $4e_g$-$e_{x^2-y^2}$ and $2b_{1u}$-e_{xy}. An important difference between the aza and methine bridges is the higher electronegativity of the former, resulting in an energetically lower-lying set of $(N)_4$ p_π orbitals. As a consequence, the final charge distribution on $(N)_4$ will be more negative and, on $(Py)_4$, more positive. This is visible in the shift in the energies of orbitals that do not interact strongly, such as the low-lying "a_1" set and the e_x set: they all shift downward due to the resulting positive charge on $(Py)_4$. This also holds for the e_y-$1a_{1u}$ which is a pure $(Py)_4$ orbital in the Pz ring system, as it is in the P ring system. We note that the N_b-based $4a_{2u}$ is no longer degenerate with the $1a_{1u}$; it is even more stabilized. This is due to the much lower energy of the N_b-based p_π orbitals than the CH p_π orbitals. The negative charging of the N_b atoms actually causes the $4a_{2u}$ to shift up considerably with respect to the initial atomic (N_b) levels, but this upward shift combined, with the downward shift of the $1a_{1u}$, is still not sufficient to bring $4a_{2u}$ close to $1a_{1u}$; there is still a considerable gap. Incidentally, the $4a_{2u}$ is not purely located at the bridging atoms; it has 47% $(N)_4$-$1a_{2u}$ character and 16%, 22%, and 15% admixtures of $1a_{2u}$, $2a_{2u}$, and $3a_{2u}$ orbitals of $(Py)_4$. This orbital, apart from its lower energy, is actually rather similar to the $4a_{2u}$ of P, with large amplitude at the bridges but also significant amplitude at the N_p atoms (see Figure 6 and the $4a_{2u}$ composition in NiP and NiPz in Table 2, Supporting Information). When comparing the Pz level scheme of Figure 5 to the level scheme of the NiPz system in Figure 2, we note that the gap between the $1a_{1u}$ and $4a_{2u}$ orbitals is even considerably enhanced in NiPz. The $4a_{2u}$ orbital in NiPz actually shifts below the $2b_{2u}$, although it is still above $3a_{2u}$, so it becomes embedded in the e_x set of orbitals. The $3e_g$ orbitals belonging to this set are stabilized strongly by the metal $4e_g$ ($3d_\pi$) so that they end up below $3a_{2u}$.

In NiPc, the effects of aza bridges and benzo rings on a_{1u} and a_{2u} orbitals are both operative. The NiPc $2a_{1u}$ is destabilized by the benzo rings but lies at somewhat lower energy than in NiTBP, due to the general downward shift of the $(BzPy)_4$-based levels induced by the aza bridges. Considering the other occupied orbital (the bridge based a_{2u}) of the four-orbital model, it is worth noting that this cannot be associated with the highest occupied a_{2u} orbital of NiPc (the $5a_{2u}$) but should be associated with the lower-lying $4a_{2u}$. The $5a_{2u}$ of NiPc is e_x^--derived. It actually has an orbital energy comparable to that of the e_x-derived $3a_{2u}$ in NiP and the e_x^-- derived $4a_{2u}$ of NiTBP (cf. Figure 2). It is higher than the e_x-based $3a_{2u}$ of NiPz since the lowering effect of the positive charging of the $(BzPy)_4$ system due to the aza bridges is compensated by the upward driving effect of the antibonding with the benzo part. The lower-lying a_{2u} orbital, the $4a_{2u}$, is the actual "Gouterman" orbital, correlating with the $4a_{2u}$ of NiP and $5a_{2u}$ of NiTBP. We refer to the plots of the $4a_{2u}$ and $5a_{2u}$ orbitals of NiPc in ref 63 (where they are denoted $1a_{2u}$ and $2a_{2u}$). These orbital plots also reveal that the $5a_{2u}$ of NiPc is actually like the NiTBP $4a_{2u}$ of Figure 6, but with an out-of-phase admixture of the NiTBP-$5a_{2u}$, to the effect that the N_p character disappears and considerable N_b character appears. This is found also in Table 2 (Supporting Information): the NiPc-$5a_{2u}$ is like the $3(4)a_{2u}$ of the other systems but with the N_p character practically reduced to zero and a considerable build up of bridge character (22.0%). Of course the NiPc $4a_{2u}$ then should be like the NiTBP $5a_{2u}$ but with an in-phase admixture of NiTBP-$4a_{2u}$, resulting in enhanced amplitude at the pyrrolic nitrogens and reduced amplitude at the bridging N_b atoms (cf. the 50%/30% distribution over pyrrolic N_p and bridge N_b for the $4a_{2u}$ of NiPc, as compared to the 26−29%/55−58% distribution of $4a_{2u}$ of the NiP, NiPz, and $5a_{2u}$ of NiTBP in Table 2).

It is interesting to note that the $4a_{2u}$ of NiPc is shifted very far down with respect to the $2a_{1u}$, due to the combined effect of upshift of $2a_{1u}$ caused by the antibonding with the benzo rings ($2a_{1u}$ is e_y^--derived) and the downshifting effect of the aza bridges on the $4a_{2u}$. As a matter of fact, $4a_{2u}$ is so low as to come very close to the e_y^+-based $1a_{1u}$. This $4a_{2u}/1a_{1u}$ (bridge/e_y^+) degeneracy is reminiscent of the extensively discussed degeneracy of the highest occupied orbitals of a_{2u}/a_{1u} (bridge/e_y) character in NiP and will receive special attention in the discussion of the excitation spectra.

Metal 3d Levels. An important feature in the level schemes of Figure 2 is the presence of the metal 3d orbitals, which are denoted by heavy lines. In the virtual spectrum, there is in all cases the $d_{x^2-y^2}$, $7b_{1g}$ in NiP and NiPz and $11b_{1g}$ in NiTBP and NiPc, which is pushed up by antibonding with the pyrrolic N_p lone pairs. The highest occupied 3d levels are the d_{z^2} ($9a_{1g}$ in NiP and NiPz and $13a_{1g}$ in NiTBP and NiPc) and the $3d_{xz,yz}$ ($4e_g$ and $6e_g$, respectively). This $3d_\pi$ is rather strongly mixed

TABLE 3: Calculated Excitation Energies (eV) and Oscillator Strengths (*f*) for the Optically Allowed ^1E_u Excited States of NiP Compared to the Experimental Data[a]

				experiment		
state	composition	exc. en.	*f*	NiP[b]	NiOEP[c]	assignment
1 ^1E_u	50%($1a_{1u}\rightarrow 5e_g$); 49%($4a_{2u}\rightarrow 5e_g$)	2.40	0.0052	2.28	2.22	Q
2 ^1E_u	42%($4a_{2u}\rightarrow 5e_g$); 42%($1a_{1u}\rightarrow 5e_g$); 8%($12e_u\rightarrow 7b_{1g}$)	3.23	1.0214	3.11	3.22	B
3 ^1E_u	96%($2b_{2u}\rightarrow 5e_g$)	3.45	0.0009			
4 ^1E_u	70%($3a_{2u}\rightarrow 5e_g$); 29%($4e_g\rightarrow 2b_{1u}$)	3.77	0.0294		3.70	N
5 ^1E_u	65%($4e_g\rightarrow 2b_{1u}$); 26%($3a_{2u}\rightarrow 5e_g$)	4.00	0.2526		4.20	L
6 ^1E_u	70%($12e_u\rightarrow 7b_{1g}$); 9%($4a_{2u}\rightarrow 6e_g$)	5.10	0.8960		5.51	EB_1
7 ^1E_u	78%($3e_g\rightarrow 2b_{1u}$); 8%($1b_{1u}\rightarrow 5e_g$)	5.31	0.1690			
8 ^1E_u	62%($1b_{1u}\rightarrow 5e_g$); 23%($2e_g\rightarrow 2b_{1u}$); 11%($3e_g\rightarrow 2b_{1u}$)	5.44	0.0001			
9 ^1E_u	87%($4e_g\rightarrow 3b_{2u}$); 7%($4a_{2u}\rightarrow 6e_g$)	5.64	0.2284			
10 ^1E_u	38%($4a_{2u}\rightarrow 6e_g$); 26%($2e_g\rightarrow 2b_{1u}$); 22%($1a_{1u}\rightarrow 6e_g$)	5.70	0.3228			
11 ^1E_u	32%($11e_u\rightarrow 7b_{1g}$); 29%($1a_{1u}\rightarrow 6e_g$); 23%($4a_{2u}\rightarrow 6e_g$)	5.79	0.0862			
12 ^1E_u	50%($11e_u\rightarrow 7b_{1g}$); 21%($1a_{1u}\rightarrow 6e_g$); 10%($4a_{2u}\rightarrow 6e_g$)	5.96	0.2092			
13 ^1E_u	99%($9a_{1g}\rightarrow 13e_u$)	6.02	0.0007			
14 ^1E_u	28%($2e_g\rightarrow 2b_{1u}$); 17%($1a_{1u}\rightarrow 6e_g$); 15%($1b_{1u}\rightarrow 5e_g$)	6.08	0.3676			

[a] The major one-electron transitions contributing to the SAOP/ALDA solution vectors are also given. [b] CS_2 solution spectrum of NiP, from ref 53. [c] Gas-phase spectrum of Ni-octaethylporphyrin (NiOEP), from ref 26.

with the lower-lying N_p-based π orbital of the macrocycle, the e_x-$3e_g$, or the e_x^--$4e_g$. The strength of the σ interaction between the tetrapyrrole N_p lone pairs and the Ni $d_{x^2-y^2}$, as well as of the out-of-plane interaction between the tetrapyrrole N_p p_z and the Ni-d_π, provide two examples of sensitivity to the macrocycle framework which are worth noting. The smaller the coordinating cavity of the macrocycle is, the stronger both these interactions, but specially the former, will be. In NiPz, where the hole size is the smallest (see Table 1, Supporting Information), the σ antibonding $7b_{1g}$ orbital is strongly destabilized and lies above the $5e_g$, and the splitting of the metal-macrocycle π bonding/antibonding pair ($3e_g/4e_g$) is relatively large. In the large-cavity macrocycle TBP, the $d_{x^2-y^2}$-$11b_{1g}$ is considerably below the e_y-$7e_g$, and the $6e_g(d_\pi)$- $4e_g(e_x^-)$ splitting is relatively small.

The remaining occupied 3d orbital, the in-plane d_{xy} orbital, is an almost purely 3d orbital in the P and TBP systems (cf. the composition of the $6b_{2g}$ in NiP and the $9b_{2g}$ in NiTBP in Table 2, Supporting Information). In the systems with aza bridges, the $3d_{xy}$ ($5b_{2g}$ in NiPz and $8b_{2g}$ in NiPc) is at considerably lower energy, being pushed down by an N_b lone pair orbital, the NiPz-$6b_{2g}$ and NiPc-$9b_{2g}$. These macrocycle orbitals are predominantly N_b lone pairs, but they also contain some N_p in-plane p_π character, which makes them suitable for in-plane π-interactions with the metal $3d_{xy}$.

An extensive discussion of all the metal−macrocycle orbital interactions has been given in a previous paper.[64]

5. Excited States and Optical Spectra

NiP. Experimentally, the spectrum of NiP has been measured in CS_2 solution in the visible and near-UV region (2.1−3.3 eV).[56] A gas-phase spectrum in a wider energy range (1.5−6.2 eV) is only available for the octaethyl-substituted nickel-porphyrin, NiOEP.[33] The two spectra are nearly identical in the common region, which is characterized by an intense feature corresponding to the B band and a very weak Q band showing two peaks ascribed to the (0−0) and (0−1) vibrational components.[33] The maximum extinction coefficients, ϵ_{max}, for the Q and B bands were estimated to be in the ratio of 1:7 from the absorption spectrum of NiOEP measured in dichloromethane solution.[33] At the higher-energy side of the Soret band, the gas-phase spectrum of NiOEP shows three bands denoted as N, L, and M (see Figure 8) and an extra band, EB_1, starting at 5.39 eV (230 nm).

The excitation energies and oscillator strengths calculated for the ^1E_u states of NiP and the experimental energy values determined from the CS_2 solution spectrum of NiP and the gas-phase spectrum of NiOEP are gathered in Table 3.

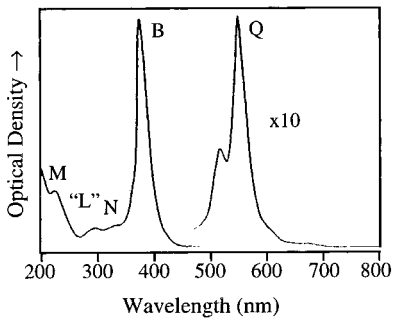

Figure 8. Gas-phase absorption spectrum of NiOEP from ref 33.

The two lowest ^1E_u states calculated at 2.40 and 3.23 eV beautifully account for the Q and B bands in the spectrum. As a consequence of the quasidegeneracy of the $1a_{1u}$ and $4a_{2u}$ orbitals, these states are a nearly 50:50 mixture of the $1a_{1u}\rightarrow 5e_g$ and $4a_{2u}\rightarrow 5e_g$ transitions. The 1^1E_u state has a very small oscillator strength (0.0052), due to the opposite directions of the two large transition dipoles ($\langle 1a_{1u}|y|5e_{g,xz}\rangle = 3.25$ au, $\langle 4a_{2u}|y|5e_{g,yz}\rangle = 2.92$ au), while the 2^1E_u where these transition dipoles are parallel has a large oscillator strength (1.0214).

The oscillator strength of the Q band is calculated to be about 200 times smaller than that of the B band, much larger than the experimentally obtained relation, even though the latter refers to the maximum extinction coefficients and not to the oscillator strengths. Although this discrepancy could be due to a vibrational enhancement of the intensity of the Q band, nevertheless one should consider that the measured extinction coefficients refer to an alkyl-substituted nickel porphyrin, while the theoretical oscillator strengths refer to the bare NiP. Calculations performed on the octamethyl substituted nickel porphyrin, NiOMP, show indeed that the alkyl substituents have the effect of increasing the intensity of the Q band, for which we obtain in the NiOMP case an oscillator strength of 0.0373, a value that is only 27 times smaller than that of the B band, in much better agreement with experiment. In the enhancement of the intensity of the Q band on going from NiP to NiOMP, one may recognize the electronic effect of the methyl groups, which, by partially removing the degeneracy of the $1a_{1u}$ and $4a_{2u}$ orbitals, cause the mixing of the $1a_{1u}\rightarrow 5e_g$ and $4a_{2u}\rightarrow 5e_g$ to be less complete (the 1^1E_u state is now composed for 60% of the $1a_{1u}\rightarrow 5e_g$ and 38% of the $4a_{2u}\rightarrow 5e_g$), so there is less complete

cancellation of the associated transition dipole moments. The intensities are obviously very sensitive to subtle chemical modification of the ring system.

The higher excited states will involve excitations out of e_x type orbitals ($2b_{2u}$, $3a_{2u}$, $3e_g$) and of course the metal d orbitals $9a_{1g}$ and $4e_g$ and, at higher energies, out of the e_y-based $2e_g$ and $1b_{1u}$ and N_p lone pair orbital $12e_u$. Of the allowed excitations out of the e_x-derived set of orbitals to $5e_g$ orbitals, the $2b_{2u} \rightarrow 5e_g$ is found purely in the 3^1E_u state calculated at 3.45 eV. The very small oscillator strength of this state is consistent with the poor on-site overlap between the purely $(Py)_4$-e_x $2b_{2u}$ orbital and the $(Py)_4$-e_y/π_{CH} antibonding $5e_g$ pointed out in the previous section. The next allowed excitation out of the e_x-derived set of orbitals to the $5e_g$, $3a_{2u} \rightarrow 5e_g$, contributes to a large extent (70%) to the 4^1E_u state, where it mixes with the lowest allowed MLCT transition of E_u symmetry, namely, the one from the Ni-d_π- $4e_g$ into the Py-e_{xy}-derived $2b_{1u}$ orbital. The next state, 5^1E_u, consists of the same transitions with approximately reversed weights. The phases of the mixing coefficients and the transition dipoles of these transitions are such that the 4^1E_u has quite low intensity due to the opposite direction of the relatively small transition dipoles (0.95 and 0.84 au for the $3a_{2u} \rightarrow 5e_g$ and $4e_g \rightarrow 2b_{1u}$, respectively), while the 5^1E_u has parallel transition dipoles and, hence, considerable intensity.

Comparing this to the experiment, we note that the very weak 3^1E_u state will be under the high-energy tail of the B band. The assignment of the fourth and fifth singlet E_u states to the N and L bands with maxima at 3.70 eV (335 nm) and 4.20 eV (295 nm) in the absorption spectrum of NiOEP is then straightforward.

The description of the N and L bands that emerges from the present calculations, involving strong participation of the MLCT transition $4e_g(3d_\pi) \rightarrow 5e_g$, leads to a reassessment of the generally accepted interpretation by Weiss et al[9] of the N and L systems in metal-porphyrins, i.e., that these states have both $\pi \rightarrow \pi^*$ character, arising from the interaction between the nearly degenerate $^1(3a_{2u}5e_g)$, and $^1(2b_{2u}5e_g)$ configurations (the numbering of the orbitals refers to NiP). According to our results, the configurational mixing occurring in the N and L states involves rather the $3a_{2u} \rightarrow 5e_g$ and $4e_g \rightarrow 2b_{1u}$ transitions, the $2b_{2u} \rightarrow 5e_g$ being completely out of business. The above mixing, however, is not complete, so the N band has a prevalent $\pi-\pi^*$ character while the L band has mainly $d_\pi \rightarrow \pi^*$ MLCT character. What we find nicely explains why the N band appears quite constant in the vapor-phase spectra of metal-porphyrins and why the L band varies considerably with the metal in both energy and intensity.

It is maybe worthwhile to mention that, at variance with the experimental evidences, at BP level the N and L bands are predicted to have $d_\pi \rightarrow \pi^*$ MLCT and $\pi-\pi^*$ character, respectively, which suggests that the MLCT states are calculated at a somewhat too low energy at BP level.

A quite large energy gap (1.1 eV) separates the 5^1E_u corresponding to the L band from the set of the remaining ^1E_u states describing the UV region of the spectrum. This region is characterized by the M band centered at 5.51 eV (225 nm), which in fact appears as a pronounced shoulder of the EB_1 extra band starting at 5.39 eV(230 nm).

As shown in Table 3, in this region we find interspersed five excited states, the 7^1E_u, 8^1E_u, 10^1E_u, 11^1E_u, and 14^1E_u calculated at 5.31, 5.44, 5.70, 5.79, and 6.08 eV respectively, with $\pi \rightarrow \pi^*$ character and four excited states, the 6^1E_u, 9^1E_u, 12^1E_u, and 13^1E_u calculated at 5.10, 5.64, 5.96, and 6.02 eV with MLCT/LMCT character. This fits in with the M band, which is

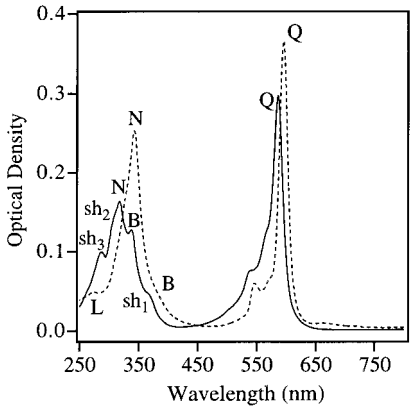

Figure 9. Absorption spectra of MgOEPz 1.2×10^{-5} M (- - -) and NiOEPz 2.5×10^{-6} M (—) in hexane at room temperature.

characteristic of the porphyrin ring and the metal-dependent EB_1 extra band being strongly overlapped. The energy of the lowest state of this set, the 6^1E_u, which is mainly a N_p (l.p.) $\rightarrow$ dσ^* state as it involves the low-lying $12e_u$ N_p lone pair orbital and the Ni $d_{x^2-y^2}$ orbital, which is characterized by a large transition moment (1.73 au, the largest after the Gouterman transitions), appears to be underestimated by our calculations. This state should contribute indeed to the intense part of the metal-dependent EB_1 extra band at higher energy than that of the M shoulder, while it is calculated to the red of the M band. Although our calculations do not allow a definitive assignment of the M band, nevertheless, the energy, intensity, and character of this band are well accounted for by the 9^1E_u (MLCT) and 10^1E_u ($\pi \rightarrow \pi^*$) excited states calculated at 5.64 and 5.70 eV with oscillator strengths of 0.2284 and 0.3228.

NiPz. Due to a rather complex synthetic pathway and to the low solubility, porphyrazines have received relatively little attention compared to the related phthalocyanines, with which they share the meso tetraaza substitution. Although the discovery of efficient synthetic routes has recently disclosed the potential of this class of tetrapyrroles,[16] the study of their physicochemical properties is still at its infancy. As for the optical spectra, gas-phase spectra of porphyrazines have not been reported so far, and the solution spectra available have been generally taken in strongly coordinating solvents and cover a rather narrow energy range (2.1−4.1 eV).[3] The nickel−porphyrazine complex, which is the object of the present investigation, does not represent an exception in this context.

To have experimental data more suitable for comparison, we have collected the optical spectrum of the newly synthesized substituted nickel−porphyrazine, NiOEPz, in a diluted solution of a noncoordinating solvent, hexane, in the range of 1.5−5.0 eV. The spectrum is displayed in Figure 9.

The visible region is dominated by an intense Q band centered at 2.1 eV (590 nm) showing vibrational structure. The ultraviolet region is characterized by a broad and structured band beginning at ∼3.0 eV (413 nm) and extending at least 2.0 eV to higher energy. It shows a weak shoulder, sh_1, at 3.30 eV (376 nm), a pronounced shoulder at 3.65 eV (340 nm) denoted according to the nomenclature used by Weiss et al.[9] as B, a main peak centered at 3.91 eV (317 nm) denoted by Weiss et al.[9] as N, and two shoulders, sh_2 and sh_3, at 4.0 eV (310 nm) and 4.29 eV(289 nm), respectively.

The excitation energies and oscillator strengths calculated for the ^1E_u states of NiPz up to 5.0 eV and the experimental energy values determined from the solution spectrum of NiOEPz are gathered in Table 4a.

The lifting of the (near) degeneracy of the $1a_{1u}$ and $4a_{2u}$

TABLE 4a: Calculated Excitation Energies (eV) and Oscillator Strengths (*f*) for the Optically Allowed ^1E_u Excited States of NiPz Compared to the Experimental Data[a]

state	composition	exc. en.	*f*	exp. NiOEPz[b]	assignment
1 ^1E_u	84%($1a_{1u} \rightarrow 5e_g$); 14%($4a_{2u} \rightarrow 5e_g$)	2.42	0.2692	2.11	Q
2 ^1E_u	97%($2b_{2u} \rightarrow 5e_g$)	3.00	0.0226	3.30	sh_1
3 ^1E_u	85%($3a_{2u} \rightarrow 5e_g$); 9%($4e_g \rightarrow 2b_{1u}$)	3.38	0.00002		
4 ^1E_u	44%($4e_g \rightarrow 2b_{1u}$); 38%($4a_{2u} \rightarrow 5e_g$); 14%($12e_u \rightarrow 7b_{1g}$); 3%($1a_{1u} \rightarrow 5e_g$)	3.51	0.1465	3.65	B
5 ^1E_u	61%($12e_u \rightarrow 7b_{1g}$); 28%($4e_g \rightarrow 2b_{1u}$)	3.67	0.0300		
6 ^1E_u	38%($4a_{2u} \rightarrow 5e_g$); 22%($12e_u \rightarrow 7b_{1g}$); 17%($4e_g \rightarrow 2b_{1u}$); 8%($1a_{1u} \rightarrow 5e_g$)	3.89	0.9220	3.91	N
7 ^1E_u	96%($3e_g \rightarrow 2b_{1u}$)	5.15	0.0051		

[a] The major one-electron transitions contributing to the SAOP/ALDA solution vectors are also given. [b] Hexane solution spectrum of Ni-octaethylporphyrazine (NiOEPz), this work.

orbitals in NiPz causes the $1a_{1u} \rightarrow 5e_g$ and $4a_{2u} \rightarrow 5e_g$ one-electron transitions to mix very little. This has important consequences for the nature and intensity of the lowest excited states. The 1^1E_u excited state is mainly (84%) described by the $1a_{1u} \rightarrow 5e_g$ transition, the $4a_{2u} \rightarrow 5e_g$ entering with only minor weight (14%). The cancellation of the transition dipoles of the $1a_{1u} \rightarrow 5e_g$ and $4a_{2u} \rightarrow 5e_g$ configurations that occurs in the lowest excited state in systems such as free-base porphin and NiP, leading to very low intensity of the Q bands, occurs to a much lesser extent in NiPz, leading, in agreement with experiment, to an intense Q band ($f = 0.2692$). The $2b_{2u} \rightarrow 5e_g$ and $3a_{2u} \rightarrow 5e_g$ configurations occur almost purely in the weak 2^1E_u and 3^1E_u excited states, respectively, at lower energy than that of the second Gouterman transition, the $4a_{2u} \rightarrow 5e_g$ (which mixes with some $1a_{1u} \rightarrow 5e_g$ and other configurations, vide infra). The low intensity of the 2^1E_u and 3^1E_u states fits in with the e_x character of the $2b_{2u}$ and $3a_{2u}$ orbitals. We note that the small change in composition of these orbitals due to the aza substitution in the ring now makes the $2b_{2u} \rightarrow 5e_g$ the more intense one of the two, leaving virtually zero transition moment for $3a_{2u} \rightarrow 5e_g$, just opposite to the situation in NiP. We assign the 2^1E_u and 3^1E_u states to the shoulder sh_1 at 3.30 eV.

Due to the downward shift of the $4a_{2u}$, the high-energy combination of the $4a_{2u} \rightarrow 5e_g$ and $1a_{1u} \rightarrow 5e_g$ excited configurations undergoes further configuration interaction with the nearly degenerate $4e_g \rightarrow 2b_{1u}$ $d_\pi \rightarrow \pi^*$ and the $12e_u \rightarrow 7b_{1g}$ N_b(l.p.) $\rightarrow$ $d\sigma^*$ excitations. (What we call "the high-energy combination of the $4a_{2u} \rightarrow 5e_g$ and $1a_{1u} \rightarrow 5e_g$, to stress the analogy with the NiP case, has actually rather little weight of $1a_{1u} \rightarrow 5e_g$, the lifting of the $1a_{1u}/4a_{2u}$ degeneracy in the porphyrazine suppressing the mixing of the Gouterman transitions to a large extent.) It should be noted that due to its bridge lone pair character, the $12e_u$ is in NiPz at much higher energy than the N_p(l.p.) $12e_u$ in NiP (see Figure 2). Three excited states result from this configurational mixing, the 4^1E_u, 5^1E_u, and 6^1E_u calculated at 3.51, 3.67, and 3.89 eV, respectively. As for the states which contain the high-energy combination of the $4a_{2u} \rightarrow 5e_g$ and $1a_{1u} \rightarrow 5e_g$ excited configurations, namely, the 4^1E_u and 6^1E_u, the phases of the mixing coefficients and the transition dipoles of the involved transitions are such that the 4^1E_u has much lower intensity ($f = 0.1465$) than that of the 6^1E_u ($f = 0.9220$). According to their energy and oscillator strength, the 4^1E_u and 6^1E_u excited states are responsible for the B and N bands, respectively.

In the region between 3.89 and 5.8 eV, we find only a weak excited state at 5.15 eV, the 7^1E_u, which is mainly described by the $3e_g \rightarrow 2b_{1u}$ $\pi \rightarrow \pi^*$ transition. Since we do not believe our calculations can be so much in error, the shoulders to the blue of the most intense UV peak, sh_2 at 4.0 eV (310 nm) and sh_3 at 4.29 eV(289 nm), should be vibrational in origin.

It should be noted that the character of the B and N bands of NiPz is very different from the character predicted by Weiss et al.[9] for these bands in the case of MgOMPz, the B and N states of NiPz involving to a large extent MLCT and LMCT transitions. The observed sensitivity to the metal of the energy and intensity of the B and N bands in transition metal porphyrazines, not observed in metal porphyrins,[33] suggests that the presence of MLCT and LMCT transitions in the B−N region is not a peculiarity of the nickel porphyrazine.

Athough the B and N bands have a different nature in transition metal and in alkaline-earth metal porphyrazines, one could nevertheless argue that they originate by the same mechanism. This is in essence the mixing of the high-energy combination of the $^1(4a_{2u}5e_g)$ and $^1(1a_{1u}5e_g)$ excited configurations, which is actually mostly $^1(4a_{2u}5e_g)$ and is raised in energy by the downward shift of the $4a_{2u}$, with the closest lying available configurations, which are of MLCT ($4e_g \rightarrow 2b_{1u}$) and LMCT ($12e_u \rightarrow 7b_{1g}$) type in nickel and presumably in other transition metal porphyrazines and of $\pi \rightarrow p^*$ type in magnesium, zinc, and free-base porphyrazines.

SCMO PPP results on MgOMPz[9] and our results on NiPz already point to this mechanism, but a definitive assessment comes from TDDFT calculations of the excited states of MgPz we have performed with the purpose of clarifying this question.

In Table 4b, the excitation energies and oscillator strengths calculated for the ^1E_u states of MgPz and the experimental energy values determined from the solution spectrum of MgOEPz shown in Figure 9 are reported. According to our results, the 3^1E_u and 4^1E_u excited states calculated at 3.31 and 3.61 eV and responsible for the B and N bands appearing in the spectrum at 3.08 eV (402 nm) and 3.74 eV (332 nm), respectively, are, as thought, a mixture of the high-energy combination of the $^1(4a_{2u}5e_g)$ and $^1(1a_{1u}5e_g)$ excited configurations with the $^1(3a_{2u}5e_g)$ $\pi-\pi^*$ configuration. One may wonder why the $^1(3a_{2u}5e_g)$ $\pi-\pi^*$ configuration mixes with the $^1(4a_{2u}5e_g)$ and $^1(1a_{1u}5e_g)$ excited configurations in MgPz but not in NiPz, where it remains pure. The reason is that in MgPz, owing to the ring deformation caused by the increased hole size of the macrocycle (the $M-N_p$ distance is 1.998 Å in MgPz and 1.894 Å in NiPz), the $4a_{2u}$ is pushed up by 0.3 eV compared to NiPz. As a consequence, the high-energy combination of the $^1(4a_{2u}5e_g)$ and $^1(1a_{1u}5e_g)$ excited configurations is at lower energy in MgPz than in NiPz and, hence, more suitable to interact with the $^1(3a_{2u}5e_g)$ configuration. The shift to lower energy of the high-energy combination of the $^1(4a_{2u}5e_g)$ and $^1(1a_{1u}5e_g)$ excited configurations on going from NiPz to MgPz is just at the origin of the red shift of the B−N system in MgPz.

The rise in energy of the $4a_{2u}$ level also causes the mixing of the $^1(4a_{2u}5e_g)$ and $^1(1a_{1u}5e_g)$ excited configurations in the 1^1E_u excited state to occur in MgPz to a slightly larger extent than in NiPz, as inferred from the composition of this state reported in panels a and b of Table 4 for NiPz and MgPz, respectively.

TABLE 4b: Calculated Excitation Energies (eV) and Oscillator Strengths (*f*) for the Optically Allowed ^1E_u Excited States of MgPz[a] Compared to the Experimental Data[a]

state	composition[b]	exp. exc. en.	*f*	MgOEPz[c]	assignment
$1\ ^1E_u$	$74\%(1a_{1u} \rightarrow 5e_g)$; $22\%(4a_{2u} \rightarrow 5e_g)$	2.34	0.2308	2.08	Q
$2\ ^1E_u$	$97\%(2b_{2u} \rightarrow 5e_g)$	2.81	0.0235		
$3\ ^1E_u$	$58\%(3a_{2u} \rightarrow 5e_g)$; $37\%(4a_{2u} \rightarrow 5e_g)$; $4\%(1a_{1u} \rightarrow 5e_g)$	3.08	0.0540	3.31	B
$4\ ^1E_u$	$39\%(4a_{2u} \rightarrow 5e_g)$; $35\%(3a_{2u} \rightarrow 5e_g)$; $19\%(1a_{1u} \rightarrow 5e_g)$	3.74	1.7084	3.61	N
$5\ ^1E_u$	$92\%(3e_g \rightarrow 2b_{1u})$	4.36	0.2290	4.52	L

[a] The major one-electron transitions contributing to the SAOP/ALDA solution vectors are also given. The calculations refer to the optimized D_{4h} structure of the molecule. Relevant geometrical parameters are the following: $Mg-N_p = 1.999$ Å; $N_p-C_\alpha = 1.371$ Å; $C_\alpha-N_b = 1.345$ Å; $C_\alpha-C_\beta = 1.463$ Å; $C_\beta-C_\beta = 1.366$ Å; $\angle C_\alpha-N_b-C_\alpha = 124.1°$; $\angle C_\alpha-N_p-C_\alpha = 108.9°$; $\angle C_\beta-C_\alpha-N_p = 108.4°$; $\angle C_\beta-C_\beta-C_\alpha = 107.2°$. [b] For ease of comparison, the same orbital numbering as that in NiPz is adopted. [c] Hexane solution spectrum of MgOEPz, this work.

A few other points are worth mentioning concerning the excited states of MgPz and NiPz.

In MgPz, the lowest excitation out of the e_x-derived set of orbitals to $5e_g$ orbitals, the $2b_{2u} \rightarrow 5e_g$, is found to not mix at all with other configurations, at variance with SCMO PPP results,[9] but in line with our results on NiPz, NiP, as well as with CASPT2 results on MgP.[65] This transition is buried under the B band in MgPz, while it results in a distinguishable shoulder, sh_1, of the B band in NiPz.

The $3e_g \rightarrow 2b_{1u}$ transition that in NiPz is found almost purely in the high-lying, very weak 7^1E_u excited state is found in MgPz to dominate a state, the 5^1E_u, that is much lower-lying and much more intense than 7^1E_u state of NiPz, as it is calculated (see Table 4b) at 4.36 eV, with an oscillator strength of 0.2290. This state nicely accounts for the band denoted as L appearing in the spectrum of MgOEPz to the blue of the N band at 4.52 eV (274 nm). That the 5^1E_u state of MgPz and the 7^1E_u state of NiPz have such different energies and intensities although they are both dominated by the $3e_g \rightarrow 2b_{1u}$ transition is understandable in the light of the different composition and energies of the e_x-derived $3e_g$ orbital in the two complexes. In MgPz, the $3e_g$ is a pure e_x-derived Pz orbital with large amplitude on N_p (35%) and C_β (57%) atoms, whereas in NiPz, the $3e_g$ is pushed to lower energy by the $3d_\pi$-$4e_g$ and acquires a 29% of metallic character at the expense of the C_β (46%) character. The decreased C_β amplitude sensibly reduces the on site overlap with the $2b_{1u}$, the resulting transition dipole moment of the $3e_g \rightarrow 2b_{1u}$ being in NiPz half that in MgPz (0.32 vs 0.69 au).

Finally, we would like to make some comments on the intensities of the main features of the electronic spectra of NiPz and MgPz.

The relative intensities of the Q,B and N bands (cf. the relative heights of the bands in Figure 9) do not seem to be well reproduced by our calculations. The stronger intensity of the N band than the B band, in particular in MgPz, is correctly reproduced, but we calculate a rather low oscillator strength for the Q band as compared to that for the N band. This does not necessarily mean, however, that the calculated oscillator strengths are incorrect.

As shown by Gouterman in the case of free base and zinc−phthalocyanines,[62] one should not compare calculated oscillator strengths to measured maximum extinction coefficients (ϵ_{max}) but, more realistically, to the experimental oscillator strengths, which are approximately proportional to the maximum extinction coefficients times the half-bandwidth, $\Delta_{1/2}$ ($f \propto \epsilon_{max}\ \Delta_{1/2}$). Given the considerable broadening of the B−N system in MgOEPz and NiOEPz, it is likely that the experimental oscillator strengths of the B, N, and Q bands, if available, would better agree with the calculated oscillator strengths than the maximum extinction coefficients do.

We also have to take into account that the calculations obviously deviate in several respects from the experimental situation. Solvent effects, which are not considered in our calculations, could influence the relative intensities of these bands, as suggested by the observed pronounced sensitivity to the solvent of the intensity and often of the energy of the main bands in metal−porphyrazines.[10] The effect of the substituents is important as well, as found in the case of NiP. Our calculations predict indeed an increase of the oscillator strength of the Q state going from NiPz to the methyl substituted nickel−porphyrazine.

NiTBP. The renaissance of work on tetrabenzoporphyrins during the last five years is certainly due to the discovery of new one-pot template synthetic methods yielding gram quantities of unsubstituted and both ring and meso-substituted species.[57,66,67] Free-base tetrabenzoporphyrin and $MgTBP(py)_2$(py = pyridine) have been recently thought to be constituents of interstellar dust,[68] which has stimulated the investigation of the spectroscopic properties of tetrabenzoporphyrins. Though now readily synthesizable, NiTBP, whose electronic spectrum is being investigated in the present work, is only slightly soluble in most noncoordinating organic solvents. It dissolves appreciably in chloroform or dichloromethane after addition of a few percent of pyridine, but optical spectra taken in these mixtures are not suitable for comparison with theoretical data, since, as recently demonstrated,[69] NiTBP axially binds two pyridine ligands. The axial coordination of the metal modifies substantially the ground-state electronic structure, and significant spectral changes are observed in the Soret band region.

To have optical spectra of NiTBP to which to compare our results, we have run a spectrum of a diluted solution of this compound in dichloromethane, in the range 1.5−5.0 eV. This spectrum is displayed in Figure 10. The visible region is dominated by a rather intense Q band centered at 2.01 eV (617 nm) showing a complex vibrational structure. The near-UV region of the spectrum is characterized by a narrow Soret (B) band at 3.00 eV (413 nm) with maximum extinction coefficient 1.7 times that of the Q band, followed by two less intense and broader absorptions centered at 3.22 eV (385 nm) and 3.60 eV (354 nm), which we label D and E, respectively. The UV region shows a very broad absorption, which, beginning from 4.0 eV (310 nm), steeply increases in intensity and shows a prominent shoulder denoted as F at 4.59 eV (270 nm).

In Table 5, the excitation energies and oscillator strengths calculated for the allowed ^1E_u states are reported together with the experimental band maxima. Just as the aza bridges, the benzo rings have the effect of removing the degeneracy of the a_{1u} and a_{2u} levels present in porphyrins; they act, however, in the opposite direction, the aza bridges depressing the a_{2u} and the benzo ring destabilizing the a_{1u}. As already discussed, the $2a_{1u}$ HOMO of NiTBP is upshifted with respect to the $1a_{1u}$ of NiP, due to the antibonding with the benzo rings ($2a_{1u}$ is e_y-derived),

TABLE 5: Calculated Excitation Energies (eV) and Oscillator Strengths (*f*) for the Optically Allowed ^1E_u Excited States of NiTBP Compared to the Experimental Data[a]

state	composition	exc. en.	*f*	experiment[b]	assignment
1 ^1E_u	82%($2a_{1u} \rightarrow 7e_g$); 17%($5a_{2u} \rightarrow 7e_g$)	2.08	0.3130	2.01	Q
2 ^1E_u	57%($5a_{2u} \rightarrow 7e_g$); 24%($2a_{1u} \rightarrow 8e_g$); 9%($2a_{1u} \rightarrow 7e_g$)	2.95	0.7144	3.00	B
3 ^1E_u	72%($2a_{1u} \rightarrow 8e_g$); 17%($5a_{2u} \rightarrow 7e_g$)	3.10	0.5354	3.22	D
4 ^1E_u	93%($3b_{2u} \rightarrow 7e_g$)	3.44	0.0021		
5 ^1E_u	74%($2b_{1u} \rightarrow 7e_g$); 13%($5a_{2u} \rightarrow 8e_g$)	3.58	0.0616		
6 ^1E_u	83%($4a_{2u} \rightarrow 7e_g$)	3.62	0.0627	~3.5	E
7 ^1E_u	83%($5a_{2u} \rightarrow 8e_g$)	3.72	0.0018		
8 ^1E_u	77%($6e_g \rightarrow 4b_{2u}$); 15%($6e_g \rightarrow 6a_{2u}$);	3.89	0.1361		
9 ^1E_u	76%($6e_g \rightarrow 6a_{2u}$); 11%($6e_g \rightarrow 4b_{2u}$)	4.03	0.2982		
10 ^1E_u	54%($1a_{1u} \rightarrow 7e_g$); 34%($6e_g \rightarrow 3b_{1u}$)	4.14	0.0702		
11 ^1E_u	55%($6e_g \rightarrow 3b_{1u}$); 34%($1a_{1u} \rightarrow 7e_g$)	4.15	0.0454		
12 ^1E_u	54%($2a_{1u} \rightarrow 9e_g$); 29%($5e_g \rightarrow 4b_{2u}$); 23%($19e_u \rightarrow 11b_{1g}$)	4.41	0.3594		
13 ^1E_u	43%($5e_g \rightarrow 4b_{2u}$); 21%($2a_{1u} \rightarrow 9e_g$)	4.48	0.2874		
14 ^1E_u	29%($2a_{1u} \rightarrow 9e_g$); 29%($19e_u \rightarrow 11b_{1g}$); 19%($18e_u \rightarrow 11b_{1g}$)	4.53	0.3802	4.59	F
15 ^1E_u	58%($5e_g \rightarrow 6a_{2u}$); 25%($2b_{1u} \rightarrow 8e_g$); 10%($5e_g \rightarrow 4b_{2u}$)	4.61	0.0244		
16 ^1E_u	71%($3b_{2u} \rightarrow 8e_g$)	4.68	0.2590		
17 ^1E_u	60%($5e_g \rightarrow 3b_{1u}$); 33%($4a_{2u} \rightarrow 8e_g$)	4.77	0.00121		
18 ^1E_u	66%($4e_g \rightarrow 4b_{2u}$); 21%($4a_{2u} \rightarrow 8e_g$);	4.85	0.0002		
19 ^1E_u	30%($4e_g \rightarrow 6a_{2u}$); 13%($4a_{2u} \rightarrow 8e_g$); 15%($2b_{1u} \rightarrow 8e_g$); 11%($18e_u \rightarrow 11b_{1g}$)	4.93	0.1102		
20 ^1E_u	40%($5a_{2u} \rightarrow 9e_g$); 30%($18e_u \rightarrow 11b_{1g}$); 13%($4e_g \rightarrow 6a_{2u}$)	4.96	0.0769		
21 ^1E_u	34%($2b_{1u} \rightarrow 8e_g$); 28%($4e_g \rightarrow 6a_{2u}$); 15%($1a_{1u} \rightarrow 8e_g$)	5.02	0.1750		
22 ^1E_u	35%($5a_{2u} \rightarrow 9e_g$); 18%($18e_u \rightarrow 11b_{1g}$); 10%($4e_g \rightarrow 3b_{1u}$); 10%($4e_g \rightarrow 6a_{2u}$)	5.15	2.212		

[a] The major one-electron transitions contributing to the SAOP/ALDA solution vectors are also given. [b] CH_2Cl_2 solution spectrum of NiTBP, this work.

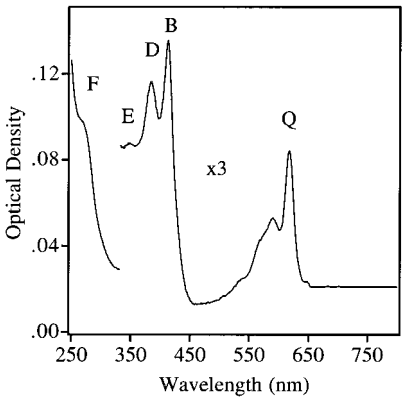

Figure 10. Absorption spectrum of NiTBP 2.5×10^{-6} M in dichloromethane at room temperature.

whereas the $5a_{2u}$ is unaffected by benzo substitution and remains mostly a $(CH)_4$ orbital. The result is that, unlike in NiP but similar to NiPz, the $2a_{1u} \rightarrow 7e_g$ and the $5a_{2u} \rightarrow 7e_g$ one-electron transitions involving the four orbitals of the four-orbital model mix very little.

The 1^1E_u excited-state calculated at 2.08 eV that is responsible for the Q band centered at 2.01 eV (617 nm) is indeed mainly (82%) described by the $2a_{1u} \rightarrow 7e_g$ transition, the $5a_{2u} \rightarrow 7e_g$ entering with only minor weight (17%). The oscillator strength associated with this state is, for the same reason as that in NiPz, quite large (0.3130), in line with the Q band being in tetrabenzoporphyrins and azaporphyrins, much more intense than in porphyrins. The upshift of the $2a_{1u}$ also causes the Q band to move slightly to the red in NiTBP compared to NiP and NiPz.

As found in NiPz, the high-energy combination of the $5a_{2u} \rightarrow 7e_g$ and $2a_{1u} \rightarrow 7e_g$ transitions, the former with the largest weight undergoes further configuration interaction. Being, however, at much lower energy than that in NiPz (both the $5a_{2u}$ and $2a_{1u}$ levels are upshifted in NiTBP compared to NiPz), it cannot mix with the too high-lying MLCT or LMCT transitions. It does so instead with the $2a_{1u} \rightarrow 8e_g$ $\pi \rightarrow \pi^*$ transition that is the lowest of the numerous $\pi \rightarrow \pi^*$ transitions enabled by the presence of additional low-lying π^* levels introduced by the benzo rings. Two intense excited states result, the 2^1E_u and the 3^1E_u calculated at 2.95 and at 3.10 eV, respectively, the former largely (57%) composed of the $5a_{2u} \rightarrow 7e_g$ and the latter dominated (72%) by the $2a_{1u} \rightarrow 8e_g$ transition. The phases of the mixing coefficients and the transition dipoles of the involved transitions are such that the 2^1E_u has higher intensity ($f = 0.7144$) than the 3^1E_u ($f = 0.5354$). The energy and intensity of the 2^1E_u and 3^1E_u excited states make unambiguous their assignment to the B band centered at 3.00 eV (413 nm) and to its shorter wavelength peak at 3.22 eV (385 nm).

The next excited states covering the energy range 3.44−3.72 eV are also of $\pi \rightarrow \pi^*$ type, but much weaker, the summed oscillator strength of these states amounting to 0.12. They involve transitions from the BzPy orbitals of the e_x^- set, the $4a_{2u}$ and the $3b_{2u}$, and from the e_y^-/e_y^+-derived $2b_{1u}$ to the $7e_g$ LUMO as well as transitions from the $(CH)_4$ based orbital, the $5a_{2u}$, to the lowest additional π^* orbital introduced by benzo rings, the $8e_g$.

All these states account for the almost flat band, E, separating the absorption at 3.22 eV (385 nm) from the broad band rising at ~3.9 eV (318 nm) and extending up to 5.0 eV (248 nm).

In the region of this broad band, we find a plethora of states, the lowest of which, the 8^1E_u, 9^1E_u, 10^1E_u, and 11^1E_u calculated at 3.89, 4.03, 4.14, and 4.15 eV, respectively, have a predominant MLCT character, involving the lowest allowed MLCT transitions of E_u symmetry, which are from the $6e_g$ d_π orbital to the low-lying π^* levels ($4b_{2u}$, $6a_{2u}$, and $3b_{1u}$). A gap of 0.3 eV separates the MLCT states from a set of closely spaced excited states spanning the region 4.41−4.68 eV. They all have $\pi \rightarrow \pi^*$ character, except for the 12^1E_u and 14^1E_u, in which the $19e_u \rightarrow 11b_{1g}$ N_p(l.p.) $\rightarrow \sigma^*$ transition enters with considerable weight. The energy and the intensity of the excited states belonging to this set nicely account for the prominent shoulder appearing in the UV region of the spectrum at 4.59 eV(270 nm).

The higher-lying excited states up to 5.15 eV involving mainly $\pi \rightarrow \pi^*$ transitions are much weaker, except for the highest, the 22^1E_u, for which a very large (2.212) oscillator

TABLE 6: Calculated Excitation Energies (eV) and Oscillator Strengths (*f*) for the Optically Allowed ^1E_u Excited States of NiPc Compared to the Experimental Data[a]

state	composition	exc. en.	*f*	experiment[b]	assignment
1^1E_u	93%($2a_{1u} \rightarrow 7e_g$)	1.97	0.6520	1.90	Q
2^1E_u	96%($3b_{2u} \rightarrow 7e_g$)	2.99	0.0244		
3^1E_u	55%($2b_{1u} \rightarrow 7e_g$); 26%($5a_{2u} \rightarrow 7e_g$); 12%($2a_{1u} \rightarrow 8e_g$); 4%($4a_{2u} \rightarrow 7e_g$)	3.16	0.00001		
4^1E_u	58%($5a_{2u} \rightarrow 7e_g$); 25%($2b_{1u} \rightarrow 7e_g$); 8%($4a_{2u} \rightarrow 7e_g$); 5%($2a_{1u} \rightarrow 8e_g$)	3.20	0.3396	~3.40[c]	B_1
5^1E_u	76%($2a_{1u} \rightarrow 8e_g$); 14%($2b_{1u} \rightarrow 7e_g$)	3.32	0.0934		
6^1E_u	87%($19e_u \rightarrow 11b_{1g}$); 8%($4a_{2u} \rightarrow 7e_g$)	3.40	0.0160		
7^1E_u	55%($1a_{1u} \rightarrow 7e_g$); 36%($4a_{2u} \rightarrow 7e_g$); 3%($5a_{2u} \rightarrow 7e_g$)	3.61	0.2254		
8^1E_u	38%($1a_{1u} \rightarrow 7e_g$); 36%($4a_{2u} \rightarrow 7e_g$); 5%($5a_{2u} \rightarrow 7e_g$);	3.85	0.4650	3.79	B_2
9^1E_u	90%($6e_g \rightarrow 3b_{1u}$)	3.91	0.0952		
10^1E_u	81%($6e_g \rightarrow 4b_{2u}$); 13%($6e_g \rightarrow 6a_{2u}$);	4.02	0.2162		
11^1E_u	80%($6e_g \rightarrow 6a_{2u}$); 9%($6e_g \rightarrow 4b_{2u}$)	4.22	0.5744	4.37	EB_1
12^1E_u	62%($5e_g \rightarrow 3b_{1u}$); 32%($2a_{1u} \rightarrow 9e_g$)	4.56	0.1437		
13^1E_u	59%($5e_g \rightarrow 4b_{2u}$); 22%($2a_{1u} \rightarrow 9e_g$); 9%($5e_g \rightarrow 6a_{2u}$)	4.63	0.0011		
14^1E_u	27%($2a_{1u} \rightarrow 9e_g$); 26%($3b_{2u} \rightarrow 8e_g$); 19%($5e_g \rightarrow 3b_{1u}$); 13%($5e_g \rightarrow 4b_{2u}$)	4.67	0.0116		
15^1E_u	48%($3b_{2u} \rightarrow 8e_g$); 39%($5a_{2u} \rightarrow 8e_g$)	4.77	0.1853		
16^1E_u	57%($5e_g \rightarrow 6a_{2u}$); 39%($2b_{1u} \rightarrow 8e_g$)	4.82	0.0005		
17^1E_u	77%($18e_u \rightarrow 11b_{1g}$); 19%($17e_u \rightarrow 11b_{1g}$)	4.94	0.2596	5.27	EB_2
18^1E_u	36%($4e_g \rightarrow 4b_{2u}$); 31%($5a_{2u} \rightarrow 8e_g$)	5.01	0.3020		
19^1E_u	73%($4e_g \rightarrow 3b_{1u}$); 11%($2b_{1u} \rightarrow 8e_g$)	5.05	0.0032		
20^1E_u	34%($4e_g \rightarrow 4b_{2u}$); 15%($4a_{2u} \rightarrow 8e_g$); 14%($4e_g \rightarrow 3b_{1u}$); 12%($2b_{1u} \rightarrow 8e_g$)	5.09	0.00004		
21^1E_u	74%($4a_{2u} \rightarrow 8e_g$)	5.15	0.0546		
22^1E_u	50%($4e_g \rightarrow 6a_{2u}$); 26%($1a_{1u} \rightarrow 8e_g$); 9%($4e_g \rightarrow 4b_{2u}$); 5%($2b_{1u} \rightarrow 8e_g$)	5.27	0.1360		
23^1E_u	85%($2b_{2u} \rightarrow 7e_g$)	5.35	0.1360		
24^1E_u	25%($17e_u \rightarrow 11b_{1g}$); 21%($16e_u \rightarrow 11b_{1g}$); 17%($4e_g \rightarrow 6a_{2u}$)	5.48	1.5268	5.69	EB_3
25^1E_u	54%($16e_u \rightarrow 11b_{1g}$); 29%($6e_g \rightarrow 3a_{1u}$)	5.51	0.1918		
26^1E_u	45%($6e_g \rightarrow 3a_{1u}$); 20%($16e_u \rightarrow 11b_{1g}$);	5.58	0.6334		
27^1E_u	78%($3a_{2u} \rightarrow 7e_g$); 9%($1a_{1u} \rightarrow 8e_g$)	5.70	0.0287		
28^1E_u	22%($1a_{1u} \rightarrow 8e_g$); 13%($3b_{2u} \rightarrow 9e_g$); 11%($3a_{2u} \rightarrow 7e_g$); 8%($2b_{1u} \rightarrow 9e_g$)	5.83	0.1116	5.90	C
29^1E_u	19%($17e_u \rightarrow 11b_{1g}$); 12%($5e_g \rightarrow 3a_{1u}$); 7%($1a_{1u} \rightarrow 8e_g$); 6%($4e_g \rightarrow 4b_{2u}$)	5.91	0.0010		
30^1E_u	41%($3b_{2u} \rightarrow 9e_g$); 26%($6e_g \rightarrow 5b_{2u}$); 20%($5a_{2u} \rightarrow 9e_g$)	6.05	0.0319		

[a] The major one-electron transitions contributing to the SAOP/ALDA solution vectors are also given. [b] Gas-phase spectra of NiPc, from ref 7. [c] Solution spectrum of NiPc, from ref 67.

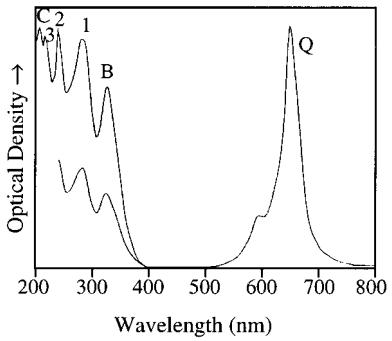

Figure 11. Gas-phase absorption spectrum of NiPc from Ref.[7]

strength is predicted, in agreement with the high intensity of the UV envelope appearing in this region of the spectrum. The large oscillator strength of this state is due to the fact that the transition dipole moments of the contributing transitions, although not particularly large being for all of them of 0.5 au, have parallel direction.

NiPc. Vapor absorption spectra in the range 2.1−6.2 eV have been reported by Edwards and Gouterman[7] for a number of metallophthalocyanines, including NiPc. The spectrum of NiPc (see Figure 11) is characterized by an intense feature in the visible identified as the Q band showing a shoulder to the blue, which is all that can be seen of the Q(0−1) vibronic band that is clearly resolved at low temperatures.[7] An intense B band is located in the near-UV region, with a maximum at 3.79 eV (327 nm). The B band shows a pronounced tail to the red region, which falls to the baseline at ~3.0 eV (413 nm). The UV spectrum of NiPc shows three "extra bands" with maxima at 4.37 eV (284 nm), 5.27 eV (235 nm), and 5.69 eV (218 nm) interpreted in terms of MLCT $d \rightarrow \pi^*$ transitions and an intense C band characteristic of the phthalocyanine ring at 5.90 eV (210 nm).

The excitation energies and oscillator strengths calculated for the lowest ^1E_u states of NiPc are compared in Table 6 with the experimental band maxima obtained from the gas-phase spectrum.[7] The excellent agreement with experiment of the calculated excitation energy and oscillator strength leaves no doubt on the assignment of the 1^1E_u state at 1.97 eV to the Q band centered at 1.90 eV (651 nm). Due to the combined effects of aza bridges and benzo rings on a_{1u} and a_{2u} orbitals, the 1^1E_u is a nearly pure (93%) $2a_{1u} \rightarrow 7e_g$ state, so the oscillator strength of this state is entirely determined by the transition dipole moment of the $2a_{1u} \rightarrow 7e_g$ transition, which is very large (4.13 au), larger than that of the corresponding $1a_{1u} \rightarrow 5e_g$ transition of NiP and NiPz. This explains why in NiPc the oscillator strength of the Q band is, in agreement with experiment, the largest along the investigated nickel−tetrapyrrole series. The downward shift of the $7e_g$ induced by the aza bridges, combined with the upshift of the $2a_{1u}$ induced by benzo rings, causes the $2a_{1u}/7e_g$ energy gap in NiPc to be the smallest among the nickel−tetrapyrroles here investigated, which fits in with the Q band being in NiPc sensibly shifted to the red (phthalocyanine solutions are blue, whereas porphyrin, porphyrazine, and tetrabenzoporphyrin solutions are red).

No more allowed excited states are calculated in the 1.97−2.99 eV energy region, which confirms the vibronic nature of the feature to the blue of the Q band with maximum at 2.08 eV (594 nm).

In the energy regime of the broad B band, we find seven excited states, three of which, the 4^1E_u, the 7^1E_u, and 8^1E_u calculated at 3.20, 3.61, and 3.85 eV, respectively, have large oscillator strength and are therefore responsible for the intensity of this band. A crucial role in the mechanism leading to these

states is played by the two valence a_{2u} orbitals of NiPc, the $5a_{2u}$ and $4a_{2u}$. The character of these orbitals has been discussed in the previous section, leading to the conclusion that it is the $4a_{2u}$ rather than the $5a_{2u}$ that should be identified as the Gouterman orbital. Due to the near-degeneracy of $5a_{2u}$ with the e_y^-/e_y^+-derived $2b_{1u}$, the $5a_{2u} \rightarrow 7e_g$ and $2b_{1u} \rightarrow 7e_g$ transitions mix in the 3^1E_u and in the previously mentioned 4^1E_u excited state where, as shown in Table 6, we find also a minor contribution from both the $4a_{2u} \rightarrow 7e_g$ and $2a_{1u} \rightarrow 7e_g$ transitions. This configuration mixing does not lead to a significant splitting of the 3^1E_u and 4^1E_u states, which are only 0.04 eV far apart, but causes their intensities to be significantly different. The phases and the magnitude of the mixing coefficients of the transitions with major weight, the $5a_{2u} \rightarrow 7e_g$ and $2b_{1u} \rightarrow 7e_g$, are indeed such that the large (2.20 au) transition dipole moment of the $5a_{2u} \rightarrow 7e_g$ and the smaller transition dipole moment of the $2b_{1u} \rightarrow 7e_g$ (1.20 au) cancel in the very weak 3^1E_u ($f = 0.000\,01$) and reinforce in the quite intense 4^1E_u ($f = 0.3396$).

As observed above, it is the $4a_{2u}$ rather than the $5a_{2u}$ that correlates with the $4a_{2u}$ of NiP and $5a_{2u}$ of NiTBP. Due to the downshifting effect of the aza bridges on the $4a_{2u}$, it is so low in NiPc as to come very close to the e_y^+-based $1a_{1u}$ (see Figure 2). This $4a_{2u}/1a_{1u}$ (bridge/e_y^+) degeneracy is reminiscent of the extensively discussed degeneracy of the highest occupied orbitals of a_{2u}/a_{1u} (bridge/e_y) character in NiP and causes the $4a_{2u} \rightarrow 7e_g$ and $1a_{1u} \rightarrow 7e_g$ transitions to undergo configuration mixing, just as the $4a_{2u} \rightarrow 5e_g$ and $1a_{1u} \rightarrow 5e_g$ are undergoing it in NiP, resulting in the 7^1E_u and 8^1E_u excited states where the $5a_{2u} \rightarrow 7_{eg}$ also enters, although with minor weight. The transition dipole moments of the $4a_{2u} \rightarrow 7e_g$ and $1a_{1u} \rightarrow 7e_g$ transitions, however, are not almost equal, but the transition dipole moment of the Gouterman-type transition $4a_{2u} \rightarrow 7e_g$ is by far larger than that of the $1a_{1u} \rightarrow 7e_g$ (1.36 vs 0.14 au). As a result, the oscillator strength of the lower-lying combination where they have opposite direction is not almost zero, but it is half that of the higher-lying combination where they have parallel direction. The oscillator strengths of the 7^1E_u and 8^1E_u excited states are indeed both quite large, amounting to 0.2254 and 0.4650, respectively. According to our calculations, the closely lying 7^1E_u and 8^1E_u excited states are responsible for the B band main peak at 3.79 eV (327 nm), denoted B_2 in Table 6, whereas the 4^1E_u accounts for the intense shoulder to the red of the B band main peak (B_1 in Table 6). This feature cannot be exactly located in the broad red tail of the B band in the gas-phase spectrum by Edwards and Gouterman,[7] but it is clearly distinguishable at ~3.4 eV (365 nm) in the solution spectrum of NiPc reported by Nakamura et al.[60] That an extra band is part of the red edge of the B band envelope has also been deduced from the MCD spectra of a number of phthalocyanines by Stillman and Nyokong,[70] who proposed to denote this band as B_1 and the main peak of the B band as B_2.

As for the remaining weak excited states computed in the red edge of the B band, the 2^1E_u and the 5^1E_u originate from $\pi \rightarrow \pi^*$ transitions, the former being a nearly pure $3b_{2u} \rightarrow 7e_g$ state and the latter being dominated by the $2a_{1u} \rightarrow 8e_g$ transition, whereas the 6^1E_u originates from the $19e_u \rightarrow 11b_{1g}$, N_b(l.p.) $\rightarrow$ dσ^* transition. Thus, except for the presence of this N_b(l.p.) $\rightarrow$ dσ^* state, the B band of NiPc has a clear $\pi \rightarrow \pi^*$ character.

Edwards and Gouterman[7] predicted that metal orbitals are involved in the excited states responsible for the extra bands of NiPc. This is confirmed by our calculations of the higher-lying excited states. In the energy regime of the first extra band centered at 4.37 eV (284 nm), we predict indeed three MLCT excited states, the 9^1E_u, 10^1E_u, and 11^1E_u, at 3.91, 4.02, and 4.22 eV, respectively. They involve transitions from the $6e_g$ d_π orbital to the low-lying π^* orbitals of the BzPy $e_{x^2-y^2}$ set. In the region of the second extra band centered at 5.27 eV (235 nm), according to our calculations, among a number of closely spaced $\pi \rightarrow \pi^*$ states, only one state, the 17^1E_u, has a LMCT character, involving N_p(l.p.) $\rightarrow$ dσ^* transitions. This suggests that the second extra band has a less pronounced metallic character than the first extra band. The 17^1E_u calculated at 4.94 eV with an oscillator strength of 0.2596 and the 18^1E_u calculated at 5.01 eV with oscillator an strength of 0.3020 provide the major contributions to the intensity of the EB_2 band.

In the energy regime of the third extra band, EB_3, centered at 5.69 eV (218 nm), we predict three excited states of mixed MLCT and LMCT character, namely, the 24^1E_u, 25^1E_u, and 26^1E_u calculated at 5.47, 5.51, and 5.58 eV, respectively, two of which, the 24^1E_u and 26^1E_u, have very large oscillator strengths. According to our calculations, the C band centered at 5.90 eV (210 nm) arises, in agreement with the observed insensitivity of its energy to the metal, from excitations involving ring orbitals, with the excited state mainly responsible for this band, the 28^1E_u calculated at 5.83 eV, having a clear $\pi \rightarrow \pi^*$ character. The summed oscillator strength of 0.1732 calculated for the C band seems to be somewhat too low compared to the summed oscillator strengths of 0.8858, 1.2336, and 2.3566 calculated for EB_1, EB_2, and EB_3 extra bands, respectively, and to the relative optical density measured for the C and the three extra bands. However, as previously stressed, only the knowledge of the experimental oscillator strengths of these bands would provide a definitive assessment of the correcteness of the calculated oscillator strengths.

6. Conclusions

Time-dependent density functional calculations have been performed on the excited states of the nickel tetrapyrrole series, NiP, NiPz, NiTBP, and NiPc. For NiPc and NiP, the theoretical results are compared to the available gas-phase spectra; for NiTBP and NiPz, comparison is made with the spectra we have collected in diluted solutions of noncoordinating solvents for NiTBP and for the newly synthesized octaethyl nickel porphyrazine, NiOEPz. The theoretical results prove to agree very well with the experimental data, providing an accurate description of the UV−vis spectra.

The effects on the optical spectra of introducing aza bridges, benzo rings, both aza bridges and benzo rings in the basic porphyrinic ring, and complexation with a transition metal ion have been highlighted and interpreted on the basis of the electronic structure changes occurring along the series. A fragment approach where the four pyrrole or indole rings and the methine or aza bridges are taken as building blocks has proven to be a very important tool not only to fully understand the electronic structure changes occurring along the investigated series, but also to predict the effects of further chemical modifications of the basic macrocycles.

The results may be summarized as follows:

(i) In NiP, the proximity of the $1a_{1u}$ and $4a_{2u}$ orbitals causes the (near-) degenerate ($1a_{1u}5e_g$) and ($4a_{2u}5e_g$) configurations to strongly mix in the 1^1E_u and 2^1E_u excited states. The phases of the mixing coefficients and transition dipoles are such that the low-energy combination occurring in the 1^1E_u state responsible for the Q band has low intensity, due to opposite directions of the two large transition dipoles, while the high-energy combination occurring in the 2^1E_u state responsible for the B band has parallel transition dipoles and therefore high intensity.

The lifting of the (near-) degeneracy of the a_{1u} and a_{2u} Gouterman orbitals to an increasing extent in the NiTBP, NiPz, and NiPc series causes the mixing between the $(a_{1u}e_g)$ and $(a_{2u}e_g)$ configurations to decrease in the same direction, almost vanishing in NiPc. The cancellation of transition dipoles that occurs in the low-energy combination of the $(a_{1u}e_g)$ and $(a_{2u}e_g)$ configurations in systems such as free-base porphin and NiP, leading to very low intensity of the Q bands, occurs to a much smaller degree in NiTBP and NiPz and does not occur at all in NiPc's where the oscillator strength of the 1^1E_u (Q) state is entirely determined by the large (4.13 au) transition dipole moment of the $2a_{1u} \rightarrow 7e_g$ transition and is, in agreement with experiment, the largest along the investigated nickel-tetrapyrrole series.

(ii) The breakdown of the (near-) degeneracy of the $(a_{1u}e_g)$ and $(a_{2u}e_g)$ configurations also causes the B band of NiTBP, NiPz, and NiPc to be different in origin from the B band of NiP and all metal−porphyrins.

The high-energy combination of the $(a_{1u}e_g)$ and $(a_{2u}e_g)$ configurations that is at the origin of the B band in NiP loses indeed the contribution of the $(a_{1u}e_g)$ configuration to an increasing extent in NiTBP, NiPz, and NiPc and, moreover, mixes with other configurations.

In NiTBP, it does so with the lowest of the numerous $\pi \rightarrow \pi^*$ transitions enabled by the presence of additional low lying π^* levels introduced by the benzo rings, the $2a_{1u} \rightarrow 8e_g$. Of the two resulting intense 2^1E_u and the 3^1E_u excited states the former is responsible for the B band, the latter for its shorter wavelength peak, the D band.

In NiPz, the high-energy combination of the $(a_{1u}e_g)$ and $(a_{2u}e_g)$ configurations it so destabilized by the downward shift of the $4a_{2u}$ that it mixes with the nearly degenerate $4e_g \rightarrow 2b_{1u}$ $d_\pi \rightarrow \pi^*$ and $12e_u \rightarrow 7b_{1g}$ N_b(l.p.) $\rightarrow$ $d\sigma^*$ excitations. Two of the resulting three excited states, the intense 6^1E_u and the relatively less intense 4^1E_u, account for the N and B bands, respectively.

In NiPc, the actual Gouterman orbital, the $4a_{2u}$, is so low as to come very close to the e_y^+-based $1a_{1u}$, causing a configuration mixing of the Gouterman configuration $(4a_{2u}7e_g)$ not with the other Gouterman configuration $(2a_{1u}7e_g)$ but with the non-Gouterman $(1a_{1u}7e_g)$ configuration. The closely lying and intense 7^1E_u and 8^1E_u excited states which result from this configurational mixing are responsible for the B band main peak (B_2). The close proximity of the higher-lying a_{2u} orbital, the $5a_{2u}$, with the $2b_{1u}$ causes, in turn, the $(5a_{2u}7e_g)$ and the $(2b_{1u}7e_g)$ configurations to mix thoroughly in the weak 3^1E_u and in the relatively intense 4^1E_u excited state, the latter accounting for the shoulder (B_1) to the red of the B band main peak.

(iii) Although the introduction of the 3d levels does not make radical changes in the absorption spectra, the d $\rightarrow$ d transitions being parity forbidden, the remarkable sensitivity to the metal of some features of the spectra fits in with the MLCT $d_\pi \rightarrow \pi^*$ and the LMCT (l.p.) $\rightarrow$ $d\sigma^*$ (either N_b-(l.p.)or N_p-(l.p.)) transitions coming into play. As a matter of fact, in NiP the L band has mainly $d_\pi \rightarrow \pi^*$ MLCT character, and in NiTBP, the region to the blue of the Soret band is dominated by numerous $d_\pi \rightarrow \pi^*$ transitions, the N_p(l.p.)$\rightarrow d\sigma^*$ LMCT transitions appearing in both cases at higher energy, namely, in the region of the M and EB_1 bands in NiP and in the region of the F band in NiTBP. In NiPz and NiPc, where the B band occurs at higher energy than in NiP and NiTBP, the low-lying N_b(l.p.) $\rightarrow$ $d\sigma^*$ LMCT transitions come into play already in the B band region, and the $d_\pi \rightarrow \pi^*$ MLCT transitions contribute to the B−N band system of NiPz and to the first extra band to the blue of the Soret band, EB_1, in NiPc.

Acknowledgment. The authors wish to thank Professor Noboru Ono (Ehime University, Matsuyama, Japan) for providing a sample of pure NiTBP, Dr. D. Favretto (CSCTCMET CNR, Padova, Italy) for performing ESI Mass Spectra, and the Laboratory of the Inorganic Department of the University of Padova for microanalyses.This research work was partially supported by the Italian MURST (Ministero dell' Università e della Ricerca Scientifica) and the Università della Basilicata, Italy (Grant 9903263473_005). We also are grateful to the National Computing facilities foundation (NCF) of The Netherlands foundation for Scientific Research (NWO) for a grant of computer time.

Supporting Information Available: Selected optimized structural data for the investigated Ni(II) tetrapyrrole series together with the recent high-quality X-ray data of NiP[56] (1 page), for the whole series, and for selected MOs an atomic orbital population analysis (2 pages). This material is available free of charge via the Internet at http://pubs.acs.org.

References and Notes

(1) Wagner, R. W.; Lindsey, J. S.; Seth, J.; Palaniappan, V.; Bocian, D. F. *J. Am. Chem. Soc.* **1996**, *118*, 3996.
(2) Reimers, J. R.; Lü, T. X.; Crossley, M. J.; Hush, N. S. *Chem. Phys. Lett.* **1996**, *256*, 353.
(3) In *Phthalocyanines: Properties and Applications*; Leznoff, C. C., Lever, A. B. P., Eds.; VCH Publishers: New York, 1990−1996; Vol. 1−4.
(4) In *The Porphyrins*; Dolphin, D., Ed.; Academic Press: New York, 1978; Vol. III, Part A.
(5) Sayer, P.; Gouterman, M.; Connell, C. R. *Acc. Chem. Res.* **1982**, *15*, 73.
(6) Weiss, C. *J. Mol. Spectrosc.* **1972**, *44*, 37.
(7) Edwards, L.; Gouterman, M. *J. Mol. Spectrosc.* **1970**, *33*, 292.
(8) Bajema, L.; Gouterman, M.; Rose, C. B. *J. Mol. Spectrosc.* **1971**, *39*, 421.
(9) Weiss, C.; Kobayashi, H.; Gouterman, M. *J. Mol. Spectrosc.* **1965**, *16*, 415.
(10) Kobayashi, N. In *Phthalocyanines: Properties and Applications*; Leznoff, C. C., Lever, A. B. P., Eds.; VCH Publishers: New York, 1993; Vol. I.; p 107.
(11) Guo, L.; Ellis, D. E.; Hoffman, B. M.; Ishikawa, Y. *Inorg. Chem.* **1996**, *35*, 5304.
(12) Liang, X. L.; Flores, S.; Ellis, D. E.; Hoffman, B. M.; Musselman, R. L. *J. Chem. Phys.* **1991**, *95*, 403.
(13) Berkovitch-Yellin, Z.; Ellis, D. E. *J. Am. Chem. Soc.* **1981**, *103*, 6066.
(14) Ellis, D. E.; Berkovitch-Yellin, Z. *J. Chem. Phys.* **1981**, *74*, 2427.
(15) Schramm, C. J.; Hoffman, B. M. *Inorg. Chem.* **1980**, *19*, 383.
(16) Fitzgerald, J.; Taylor, W.; Owen, H. *Synthesis* **1991**, 686.
(17) Nakatsuji, H.; Hasegawa, J.; Hada, M. *J. Chem. Phys.* **1996**, *104*, 2321.
(18) Toyota, K.; Hasegawa, J.; Nakatsuji, H. *Chem. Phys. Lett.* **1996**, *250*, 437.
(19) Toyota, K.; Hasegawa, J.; Nakatsuji, H. *J. Phys. Chem. A* **1997**, *101*, 446.
(20) Hashimoto, T.; Choe, Y.-K.; Nakano, H.; Hirao, K. *J. Phys. Chem. A* **1999**, *103*, 1894.
(21) Casida, M. In *Recent Advances in Density Functional Methods*; Chong, D. P., Ed.; World Scientific: Singapore, 1995; Vol. 1, p 155.
(22) Casida, M. E. In *Recent Developments and Applications of Modern Density Functional Theory*; Seminario, J. M., Ed.; Elsevier: Amsterdam, 1996.
(23) Petersilka, M.; Gossmann, U. J.; Gross, E. K. U. *Phys. Rev. Lett.* **1996**, *76*, 1212.
(24) Petersilka, M.; Gross, E. K. U. *Int. J. Quantum Chem. Symposia* **1996**, *30*, 181.
(25) Jamorski, C.; Casida, M.; Salahub, D. R. *J. Chem. Phys.* **1996**, *104*, 5134.
(26) Bauernschmitt, R.; Ahlrichs, R. *Chem. Phys. Lett.* **1996**, *256*, 454.
(27) Stratmann, R. E.; Scuseria, G. E.; Frisch, M. J. *J. Chem. Phys.* **1998**, *109*, 8218.
(28) Bauernschmitt, R.; Ahlrichs, R.; Hennrich, F. H.; Kappes, M. M. *J. Am. Chem. Soc.* **1998**, *120*, 5052.
(29) van Gisbergen, S. J. A.; Groeneveld, J. A.; Rosa, A.; Snijders, J. G.; Baerends, E. J. *J. Phys. Chem. A* **1999**, *103*, 6835.
(30) Rosa, A.; Baerends, E. J.; van Gisbergen, S. J. A.; van Lenthe, E.; Groeneveld, J. A.; Snijders, J. G. *J. Am. Chem. Soc.* **1999**, *121*, 10356.

(31) van Gisbergen, S. J. A.; Rosa, A.; Ricciardi, G.; Baerends, E. J. *J. Chem. Phys.* **1999**, *111*, 2505.
(32) Ricciardi, G.; Rosa, A.; van Gisbergen, S. J. A.; Baerends, E. J. *J. Phys. Chem. A* **2000**, *104*, 635.
(33) Edwards, L.; Dolphin, D. H.; Gouterman, M. *J. Mol. Spectrosc.* **1970**, *35*, 90.
(34) Baerends, E. J.; Gritsenko, O. V.; van Leeuwen, R. In *Chemical Applications of Density Functional Theory*; Laird, B. B., Ross, R. B., Ziegler, T., Eds.; American Chemical Society: Washington, DC, 1996; Vol. 629, pp 20−41.
(35) Baerends, E. J.; Gritsenko, O. V. *J. Phys. Chem. A* **1997**, *101*, 5383−5403.
(36) Süle, P.; Gritsenko, O. V.; Nagy, A.; Baerends, E. J. *J. Chem. Phys.* **1995**, *103*, 10085−10094.
(37) Gritsenko, O. V.; van Leeuwen, R.; Baerends, E. J. *J. Chem. Phys.* **1994**, *101*, 8955−8963.
(38) Bickelhaupt, F. M.; Baerends, E. J. In *Reviews in Computational Chemistry*; Lipkowitz, K. B., Boyd, D. R., Eds.; Wiley: New York, 2000; Vol. 15, pp 1−86.
(39) Gross, E. K. U.; Kohn, W. *Adv. Quantum Chem.* **1990**, *21*, 255.
(40) Gross, E. U. K.; Dobson, J. F.; Petersilka, M. In *Density Functional Theory, Springer Series " Topics in Current Chemistry"*; Nalewajski, R. F., Ed.; Springer: Heidelberg, 1996.
(41) Gross, E. K. U.; Ullrich, C. A.; Gossmann, U. J. NATO ASI Series B; Plenum: New York, 1995; Vol. 337, p 149.
(42) van Gisbergen, S. J. A.; Snijders, J. G.; Baerends, E. J. *J. Chem. Phys.* **1995**, *103*, 9347.
(43) van Gisbergen, S. J. A.; Snijders, J. G.; Baerends, E. J. *Comput. Phys. Commun.* **1999**, *118*, 119.
(44) van Gisbergen, S. J. A.; Snijders, J. G.; Baerends, E. J. *Phys. Rev. Lett.* **1997**, *78*, 3097−3100.
(45) van Gisbergen, S. J. A.; Snijders, J. G.; Baerends, E. J. *J. Chem. Phys.* **1998**, *109*, 1064.
(46) Vosko, S. H.; Wilk, L.; Nusair, M. *Can. J. Phys.* **1980**, *58*, 1200.
(47) Bauernschmitt, R.; Häser, M.; Treutler, O.; Ahlrichs, R. *Chem. Phys. Lett.* **1997**, *264*, 573.
(48) Gritsenko, O. V.; Schipper, P. R. T.; Baerends, E. J. *Chem. Phys. Lett.* **1999**, *302*, 199.
(49) Schipper, P. R. T.; Gritsenko, O. V.; van Gisbergen, S. J. A.; Baerends, E. J. *J. Chem. Phys.* **2000**, *112*, 1344.
(50) Becke, A. *Phys. Rev. A* **1988**, *38*, 3098.
(51) Perdew, J. P. *Phys. Rev. B* **1986**, *33*, 8822 (Erratum: **Phys. Rev. B** *34*, **1986**, 7406).
(52) Baerends, E. J.; Ellis, D. E.; Ros, P. *Chem. Phys.* **1973**, *2*, 41.
(53) te Velde, G.; Baerends, E. J. *J. Comput. Phys.* **1992**, *99*, 84.
(54) Fonseca Guerra, C.; Visser, O.; Snijders, J. G.; te Velde, G.; Baerends, E. J. In *Methods and Techniques for Computational Chemistry*; Clementi, E., Corongiu, G., Eds.; STEF: Cagliari, 1995; pp 305−395.
(55) ADF STO basis set database available on line at http://tc.chem.vu.nl/SCM/Doc/atomicdatabase.
(56) Jentzen, W.; Turowska-Tyrk, I.; Scheidt, W. R.; Shelnutt, J. A. *Inorg. Chem.* **1996**, *35*, 3559.
(57) Ito, S.; Murashima, T.; Uno, H.; Ono, N. *Heterocycles*, in press.
(58) Gouterman, M. *J. Chem. Phys.* **1959**, *30*, 1139.
(59) Baerends, E. J.; Rosa, A.; Ricciardi, G. Manuscript in preparation.
(60) Simpson, W. T. *J. Chem. Phys.* **1949**, *17*, 1218−1221.
(61) Platt, J. R. In *Radiation Biology*; Hollaender, A., Ed.; McGraw-Hill: New York, 1956; Vol. 3, pp 71−123.
(62) Gouterman, M. *J. Mol. Spectrosc.* **1961**, *6*, 138.
(63) Rosa, A.; Baerends, E. J. *Inorg. Chem.* **1993**, *32*, 5637.
(64) Rosa, A.; Baerends, E. J. *Inorg. Chem.* **1994**, *33*, 584−595.
(65) Rubio, M.; Roos, B. O.; Serrano-Andrés, L.; Merchán, M. *J. Chem. Phys.* **1999**, *15*, 7202.
(66) Vicente, M. G. H.; Tomé, A. C.; Walter, A.; Cavaleiro, J. A. S. *Thetrahedron Lett.* **1997**, *38*, 3639.
(67) Ito, S.; Ochi, N.; Murashima, T.; Uno, H.; Ono, N. *J. Chem. Soc., Chem. Commun.* **1998**, 1661.
(68) Johnson, F. M. *The Diffuse Interstellar Bands*; Cluwer: Boston, 1995.
(69) Cromer, S.; Hambright, P.; Grodkowski, J.; Neta, P. *J. Porphyrins Phthalocyanines* **1997**, *1*, 45.
(70) Stillman, M. J.; Nyokong, T. N. In *Phthalocyanines: Properties and Applications*; Leznoff, C. C., Lever, A. B. P., Eds.; VCH Publishers: New York, 1989; Vol. I, Chapter 3, pp 133−289.